



Reversible and Irreversible Time-Dependent Behavior of GRCop-84

Bradley A. Lerch, Steven M. Arnold, and David L. Ellis
Glenn Research Center, Cleveland, Ohio

NASA STI Program . . . in Profile

Since its founding, NASA has been dedicated to the advancement of aeronautics and space science. The NASA Scientific and Technical Information (STI) Program plays a key part in helping NASA maintain this important role.

The NASA STI Program operates under the auspices of the Agency Chief Information Officer. It collects, organizes, provides for archiving, and disseminates NASA's STI. The NASA STI Program provides access to the NASA Technical Report Server—Registered (NTRS Reg) and NASA Technical Report Server—Public (NTRS) thus providing one of the largest collections of aeronautical and space science STI in the world. Results are published in both non-NASA channels and by NASA in the NASA STI Report Series, which includes the following report types:

- **TECHNICAL PUBLICATION.** Reports of completed research or a major significant phase of research that present the results of NASA programs and include extensive data or theoretical analysis. Includes compilations of significant scientific and technical data and information deemed to be of continuing reference value. NASA counter-part of peer-reviewed formal professional papers, but has less stringent limitations on manuscript length and extent of graphic presentations.
- **TECHNICAL MEMORANDUM.** Scientific and technical findings that are preliminary or of specialized interest, e.g., “quick-release” reports, working papers, and bibliographies that contain minimal annotation. Does not contain extensive analysis.
- **CONTRACTOR REPORT.** Scientific and technical findings by NASA-sponsored contractors and grantees.
- **CONFERENCE PUBLICATION.** Collected papers from scientific and technical conferences, symposia, seminars, or other meetings sponsored or co-sponsored by NASA.
- **SPECIAL PUBLICATION.** Scientific, technical, or historical information from NASA programs, projects, and missions, often concerned with subjects having substantial public interest.
- **TECHNICAL TRANSLATION.** English-language translations of foreign scientific and technical material pertinent to NASA's mission.

For more information about the NASA STI program, see the following:

- Access the NASA STI program home page at <http://www.sti.nasa.gov>
- E-mail your question to help@sti.nasa.gov
- Fax your question to the NASA STI Information Desk at 757-864-6500
- Telephone the NASA STI Information Desk at 757-864-9658
- Write to:
NASA STI Program
Mail Stop 148
NASA Langley Research Center
Hampton, VA 23681-2199



Reversible and Irreversible Time-Dependent Behavior of GRCop-84

Bradley A. Lerch, Steven M. Arnold, and David L. Ellis
Glenn Research Center, Cleveland, Ohio

National Aeronautics and
Space Administration

Glenn Research Center
Cleveland, Ohio 44135

Acknowledgments

This work was supported by NASA Glenn Research Center under the Higher Operating Temperature Propulsion Components (HOTPC) Program, program manager Carol Ginty, and the Second Generation Reusable Launch Vehicle Program, program manager Margret Tuma. Support for the documentation of this work was provided by NASA's Low Cost Upper Stage-Class Propulsion (LCUSP), project lead John Fikes.

Trade names and trademarks are used in this report for identification only. Their usage does not constitute an official endorsement, either expressed or implied, by the National Aeronautics and Space Administration.

Level of Review: This material has been technically reviewed by technical management.

Available from

NASA STI Program
Mail Stop 148
NASA Langley Research Center
Hampton, VA 23681-2199

National Technical Information Service
5285 Port Royal Road
Springfield, VA 22161
703-605-6000

This report is available in electronic form at <http://www.sti.nasa.gov/> and <http://ntrs.nasa.gov/>

Reversible and Irreversible Time-Dependent Behavior of GRCo-84

Bradley A. Lerch, Steven M. Arnold, and David L. Ellis
National Aeronautics and Space Administration
Glenn Research Center
Cleveland, Ohio 44135

Summary

A series of mechanical tests were conducted on a high-conductivity copper alloy, GRCo-84, in order to understand the time-dependent response of this material. Tensile, creep, and stress relaxation tests were performed over a wide range of temperatures, strain rates, and stress levels to excite various amounts of time-dependent behavior. At low applied stresses the deformation behavior was found to be fully reversible. Above a certain stress, termed the viscoelastic threshold, irreversible deformation was observed. At these higher stresses the deformation was observed to be viscoplastic. Both reversible and irreversible regions contained time-dependent deformation. These experimental data are documented to enable characterization of constitutive models to aid in the design of high-temperature components.

Introduction

GRCo-84 is a high-performance copper-based ternary alloy designed for extended high-temperature applications such as regeneratively cooled rocket engine liners. The copper matrix is dispersion strengthened by the intermetallic Laves phase compound Cr_2Nb . This high-melting-point intermetallic compound is stable and does not undergo much growth, even during high-temperature thermal exposures. The result is excellent retention of strength and other properties well past temperatures attainable for precipitation-strengthened copper alloys such as Cu-Cr and Cu-Zr. The stability, combined with the excellent elevated-temperature properties, makes GRCo-84 and other Cu-Cr-Nb alloys highly attractive for applications involving high thermal loads such as reusable launch vehicle engines. Its good resistance to mechanical and thermal fatigue is an advantage for an engine that may undergo hundreds of firings between overhauls.

The GRCo-84 alloy was developed at NASA's Glenn Research Center starting in the 1980s (Ellis and Michal, 1989). Since then a number of studies have been performed on this material to understand its capabilities and behavior and to optimize its processing for use. A description of the basic chemistry and microstructure of GRCo-84 is given in the report by Ellis (2005). Work was performed on processing to examine rolling parameters on select mechanical properties (Loewenthal and Ellis, 2008), showing that a wide range of processing conditions can be used without significantly influencing the properties. The thermophysical properties of GRCo-84 were measured over a wide temperature range and presented by Ellis, Keller, and Nathal (2000). It was shown that while alloying resulted in decreases in both thermal and electrical conductivity compared to pure copper, GRCo-84 had a lower thermal expansion. Since the expansion of GRCo-84 is closer to that of the nickel structural jacket wrapping the combustion chamber, this should result in lower thermal stresses during high-temperature service. Since this alloy was developed for rocket engines, its sensitivity to high-pressure hydrogen was investigated in Ellis and Hastings (2006) and shown that exposure to hydrogen resulted in minimal changes in mechanical properties. Some work has been performed on its oxidation behavior (Thomas-Ogbuji and Humphrey, 2000) and on coating development (Raj et al., 2006). The basic thermal-mechanical properties have been reported in Ellis, Loewenthal, and Yun (2012) and in Loewenthal and Ellis (2011), and summarized in the Aerospace Structural Materials Database (Ellis, 2002). The properties of GRCo-84 have been compared upon variations on the basic composition (Ellis and Michal, 1989), particularly GRCo-42 (Ellis and Michal, 1996; and Loewenthal and Ellis, 2011) as well as two other copper alloys (de Groh, Ellis, and Loewenthal, 2007). Although many of these articles on GRCo-84 present basic mechanical properties at

elevated temperature, none of them focus on their time dependency. Therefore, the current work is aimed at identifying the viscoelastoplastic, nonlinear behavior of the material, which is important in describing its high-temperature thermal-mechanical deformation and life behavior.

Because of the relatively high service temperatures associated with rocket applications and the likely thermal cycling that components are exposed to, an understanding of the hereditary (i.e., path and time-dependence) behavior of GRCop-84 is desirable. Consequently, a test plan was designed to provide suitable characterization data for a viscoelastoplastic constitutive model. The specific model of interest was the Generalized Viscoplasticity with Potential Structure (GVIPS) model put forth by Arnold and Saleeb, see Arnold et al. (2001, 2009, and 2014), Saleeb et al. (2001), and Saleeb and Arnold (2001 and 2004). This model is a comprehensive viscoelastoplastic constitutive model that aims to describe the material's behavior whether in the viscoplastic or viscoelastic region. To provide the data required to characterize and validate the model, a series of tests based upon the then-current best understanding of the model and materials' response was undertaken. While this model provides the motivation for the types of tests conducted herein, the data can be used with any other constitutive model for describing tensile, creep, relaxation, and other high-temperature, rate-dependent loading conditions. Portions of the data (e.g., the tensile and creep results) can also be used for the design of rocket engine combustion chamber liners, the intended application, and other parts.

Based on the GVIPS model, stresses below an explicit limit value (threshold) defines a region where the material deforms by viscoelastic mechanisms, enabling all time-dependent deformation to be fully recovered upon load reversal. The boundary between reversible viscoelastic and irreversible viscoplastic deformation is defined by a threshold shear stress value termed kappa, κ , or in the case of applied uniaxial stress, Y , wherein a J_2 formulation (Ibrahimbegovic, 2009) $Y = \sqrt{3} * \kappa$ is assumed. For stress values above the threshold both reversible and irreversible deformation coexist.

This model has been used to describe the deformation behavior in two titanium alloys (Ti-6-4 and Timetal 21S) and a nickel-base turbine disc alloy ME3. Initial work on Timetal 21S (Saleeb and Arnold, 2001 and Arnold, Saleeb, and Castelli, 2001) indicated a viscoelastic regime in which deformation was completely reversible. Moreover the initial modulus was shown to be rate dependent, particularly at higher test temperatures. Lerch and Arnold (2014) performed an extensive characterization on the viscoelastoplastic behavior of Ti-6Al-4V over the temperature range of 20 to 538 °C where similar viscoelastic behavior was observed. They also showed that the viscoelastic threshold stress was nearly equivalent to the apparent proportional limit at a very slow (e.g., 10^{-06} s^{-1}) rate of loading. Additional work by the authors on ME3 also indicated the existence of viscoelastic behavior. This is apparently not unusual as Sinha (2001 and 2005) has observed viscoelasticity (anelastic, or recovery, strain) in several other Ni-based superalloys.

For Ti-6-4 Lerch and Arnold (2014 and 2016) performed an extensive array of tests over a wide range of parameters to fully describe its time-dependent (both viscoelastic and viscoplastic) behavior. However, GRCop-84 was studied earlier when views on characterizing the GVIPS model were in their infancy. Much less testing was conducted on the GRCop-84 as it was felt at that time that the approach should focus heavily on a single reference temperature, and only limited tests were performed at other temperatures; specifically, one at a higher and one at a lower temperature. The thought was that at temperatures below the reference, the material deformation would be dominated by rate-independent (elastic-plastic) behavior. Above the reference temperature, rate- and time-dependent (viscoelastoplastic) behavior would dominate. During the more recent Ti-6Al-4V program, it was found that multiple temperatures should be equally characterized over the temperature range of interest. This is particularly important to aid in the consistent characterization of the nonlinear model over a wide temperature range. Moreover, testing should employ various loading rates to engage varying degrees of time-dependent deformation. Step and block tests should be used for exploring history-dependent deformation, and dwell times and overloads used for characterizing interaction effects. Such extensive testing was not done for the GRCop-84, unfortunately, and the number of loading rates examined were limited.

Although perhaps insufficient to develop a fully validated GVIPS model, the current data set provides considerable insight into the behavior of GRCop-84. This has become important in recent years, as GRCop-84 is being baselined for various rocket applications such as NASA's Low Cost Upper Stage-Class Propulsion project. The data represent a significant portion of currently existing data describing the high-temperature, nonlinear behavior of GRCop-84. It has not been previously reported in the open literature, but should prove useful for initial design purposes and for comparison with future tests conducted based on additively manufactured coupons. The data consist of tensile, creep, and stress relaxation tests in both the viscoelastic and viscoplastic deformation regimes. These tests were conducted at low to intermediate stresses, and samples were generally not taken to failure: they were designed to assess deformation behavior only.

Experimental Details

GRCop-84 bar stock was manufactured from extruded powder. Three extrusions (labeled as C199, C200, and C201) were made from the powder designated as Lot 1. The chemical composition is given in Table I. The material was reported (Ellis, Carter, and Ferry, 2015) to have an average grain size of 1.65 μm and a strong duplex fiber texture, as well as a dominant rotated recrystallization cube texture. Cylinders of 57 mm lengths were cut from the extruded bars. To minimize thermal gradients in the elevated-temperature tests, 316 stainless steel cylinders were inertia welded to both ends of the GRCop-84 cylinders. This minimized the heat flow from the highly conductive GRCop-84 into the water-cooled test grips and provided a more suitable temperature gradient over the sample's gage length. The final machined test sample is shown in Figure 1 with nominal dimensions given in Figure 2. Samples were tested in the as-extruded condition with the exception of four samples in which a thermal treatment—to simulate a typical brazing run for joining the liner to its jacket—was applied.

Samples were tested in a hydraulic load frame that included an environmental chamber. The chamber was evacuated with a mechanical pump to approximately 13.3 Pa (100 millitorr) and then backfilled with ungettered, 99.995 percent purity argon. A constant flow of 2 lpm of argon was maintained throughout all tests at elevated temperatures to maintain a slightly positive chamber pressure with respect to atmospheric pressure. This procedure prevented gross oxidation of the samples at elevated temperatures.

Samples were heated using induction heating. The temperature was measured using a 32-gauge type R thermocouple. Test temperatures of 20, 200, 400, and 600 $^{\circ}\text{C}$ were used. One sample was tested at 500 $^{\circ}\text{C}$. The temperature gradient was ± 2.7 percent at 200 $^{\circ}\text{C}$ and decreased as the temperature increased. After reaching the desired test temperature, the load cell was tared, and the bottom of the sample was gripped.

Based upon the type of test being conducted, tests were run using either strain or load control. Various strain rates (or elastic equivalent load rates) were used from 3×10^{-6} to $5 \times 10^{-4} \text{ s}^{-1}$. Strain was measured using a high-temperature, 13-mm-gage-length extensometer. They employed 150-mm-long alumina probes to contact the sample surface. The probes were spring loaded with a 100g force to maintain contact with the sample. The extensometer was cooled with the argon used for backfilling the environmental chamber. Tensile tests were conducted in strain control and typically run until the stress saturated at near-ultimate load. For both creep and relaxation tests the planned hold time was 24 h. For several reasons, the actual dwell times were often shorter than the 24-h period. After each test type was complete, the samples were unloaded at the same rate used during loading to zero load¹ and held for a 24-h recovery period. This was done in an attempt to recover all reversible strain, leaving only the irreversible, permanent part.

¹For strain-controlled tests (such as stress relaxation), the control mode was automatically switched to load control upon reaching zero load and then recovered.

A few dynamic modulus tests were conducted on samples machined from the extruded bars. The samples were parallelepipeds, 30×4×2.4 mm in size. The tests were conducted using the impact vibration method from ASTM E1876 (ASTM 2009). The tests were conducted from 28 to 800 °C in argon with data collected every 10 °C. The measured modulus was parallel to the axis of the extruded bar.

Results

The complete test matrix for this study is given in Table II, which includes the test type, test conditions, and resulting tensile properties.

Viscoelastic Tests

A series of tests were run at low stress levels (below the threshold stress Y) at 200 and 400 °C to provide characterization data for the viscoelastic model. Figure 3 depicts two creep tests at 200 °C using an elastic strain rate of $1 \times 10^{-4} \text{ s}^{-1}$. Both stress levels are below the samples' proportional limits, yet exhibit some small amount of time dependence (i.e., creep). Although not shown here, small amounts (25 percent of elastic load-up strain) of creep were also observed for tests at 20 °C. Figure 4 shows the axial strain as a function of time. Small amounts of primary creep were observed in the lower stress test, and time-dependent recovery was observed after unloading to zero stress. Note that the strains fully recover to zero in this test. At the higher stress level more primary creep was observed. After its recovery, a nonzero strain (75 microstrain) was still observed, indicating that the deformation is not completely reversible. Hence at this stress level, the sample exceeds its threshold and exhibited some viscoplastic behavior. In Figure 3 the range of threshold stress is indicated by the gray shading. The threshold equivalent in strain space (Fig. 4) is shown by $\varepsilon_{\max}^R = Y/E_S$ (where E_S is the infinitely slow modulus, the material stiffness when loaded at an extremely slow rate), which represents the maximum reversible strain achievable after infinite time.

Creep tests shown in Figure 5 were conducted at 400 °C. The creep stress was below the proportional limit for every test with the exception of sample C201-9b, which was tested at the highest stress (69 MPa). The creep stress for this sample was slightly greater (by approximately 10 percent) than its proportional limit of 61 MPa. This sample and sample C201-18 (34.9 MPa) were both tested above the viscoelastic threshold, Y , and incurred irreversible deformation. This can be more easily observed in Figure 6, where the strains are plotted over time. Both of the high-stress samples recover only to a strain of 300 to 330 $\mu\epsilon$ and would never fully recover to zero strain in any reasonable time. Note that the 300- $\mu\epsilon$ level exceeds the 100- $\mu\epsilon$ delimitation previously arrived at for defining whether or not a test exceeded the threshold (Lerch and Arnold, 2014).

Two relaxation tests were also conducted at 400 °C and are shown in Figures 5 (stress-strain space) and 7 (stress-time space). The relaxation and recovery times for these two tests were only 18 h. Both tests were below the viscoelastic threshold. Sample C201-9 was recovered at zero load and the strain remained fairly constant at a value of 30 $\mu\epsilon$. The second sample, C201-9a, was unloaded to zero strain and recovered through stress relaxation. The final stress value after 18 h of recovery was 4 MPa (15 percent of the maximum stress). Both of these samples can be considered within experimental scatter to be fully reversible. Both samples exhibit time dependency at stress relaxation values below their proportional limits. In agreement with expected viscoelastic behavior, the strains after unloading return to near-zero values.

Values for E_S were calculated by using the strains and stresses at saturation of either the creep strain or the relaxation stress. This process is described in detail in Lerch and Arnold, (2014). E_S represents a line fitted to all of the final stress-strain points reached at shutdown of the viscoelastic process and represents the stiffness that would be present if the material were loaded at an infinitely slow speed. Therefore E_S becomes the lower limit on stiffness. The other key viscoelastic parameter, Y , the uniaxial

threshold stress, was calculated using the viscoelastic subtraction method (under creep) as suggested by Arnold, Saleeb, and Castelli (2001).

$$Y = \bar{\sigma} - E_S \epsilon^{\text{IR}} \quad (1)$$

where $\bar{\sigma}$ is the applied stress level (just below the value of the proportional limit, PL , for a high-strain-rate test but above the threshold stress) where the creep test was held and ϵ^{IR} is the irreversible strain (permanent deformation) determined after unloading and allowing sufficient time for all recovery to take place. Note that the threshold stress in shear is related to Y by the following expression, assuming a J2 theory:

$$\kappa = \frac{Y}{\sqrt{3}} \quad (2)$$

The values for Y and E_S are given in Table III along with sample tensile properties.

The infinitely slow modulus E_S is plotted in Figure 8 as a function of temperature. Clearly, E_S decreases with increasing temperature and decreases at a rapid rate above 400 °C. Similar behavior was previously shown for two different Ti alloys (see Arnold, Saleeb, and Castelli, 2001; and Lerch and Arnold, 2014). Also plotted in this figure is a curve representing dynamic stiffness measured using the impact vibration method. These values represent an upper limit on stiffness for very fast rates and show much less degradation with increasing temperature. There are also data indicated by discrete symbols. These are stiffnesses measured on individual samples using tensile testing and with various loading rates. Stiffnesses representing another data set given by the open symbols were conducted on one sample but between very small (± 14 MPa) stresses, but over a wide range of rates and temperatures. Finally, the filled symbols represent average modulus from a number of samples tested under tensile loading at those specific conditions. There is a curve drawn to represent the average stiffness for samples having a loading rate² of $1 \times 10^{-4} \text{ s}^{-1}$. The important conclusion from this figure is that the material stiffness is not only temperature, but loading rate dependent. The rate dependence becomes larger at higher temperatures but exists to a lesser extent even at lower temperatures (< 200 °C). The lowest possible stiffness (representing an infinitely slow rate) is given by E_S , which is 92 percent lower than the dynamic modulus at a temperature of 600 °C.

Figure 9 illustrates the corresponding deformation modeling map for GRCo-84 wherein the threshold stress, dynamic modulus, and infinitely slow modulus are plotted as a function of temperature. Similar maps have been shown for Ti-6-4, Timetal 21S, and ME-3 materials (see Arnold, Lerch, and Sellers, 2013; Arnold et al., 2013 and 2014; and Lerch and Arnold, 2014). Values for E_S were supplemented with calculations from samples tested above the threshold but which were still unloaded and recovered. For these samples, E_S was calculated from the viscoelastic recovery that occurred after unloading. This method yielded many more data points than by only using data from those samples tested below the threshold. Both sets of values are consistent with one another. For GRCo-84, the material was rate dependent above room temperature. This was in contrast to Ti-6Al-4V, which did not show significant rate dependence until a temperature of 300 °C (Lerch and Arnold, 2014). For stress levels below the GRCo-84 threshold Y all deformation was viscoelastic and reversible. For stress levels above the threshold the deformation was irreversible and rate dependent (i.e., viscoelastoplastic). It should be noted in Figure 9 that the rate and time dependency begins at a homologous temperature, $T/T_m = 0.22$,

²A strain rate of $1 \times 10^{-4} \text{ s}^{-1}$ was used for the bulk of the tests in this study. Later tests for characterizing the GVIPS model used a faster strain rate of $1 \times 10^{-3} \text{ s}^{-1}$, as the faster rate had a better chance of “locking in” time dependency during loading. In hindsight, a faster rate would have been more effective for the GRCo-84 tests.

where T_m represents the melting point. Traditionally, materials are known to be rate and time dependent when the homologous temperature is equal to or above 0.25, and this is consistent with the behavior of the GRCop-84. Ti-6Al-4V was shown to exhibit rate dependence above $T/T_m = 0.29$ (Lerch and Arnold, 2014) and also satisfies this guideline.

Viscoplastic

This section describes tests at stress levels above the viscoelastic threshold. Thus all of these samples experienced irreversible, permanent deformation.

Tensile

Figure 10 depicts the tensile behavior at 20 °C for three different samples tested at a strain rate of approximately $1 \times 10^{-4} \text{ s}^{-1}$, and the curves show good agreement. The viscoelastic threshold and proportional limits are also plotted, and for each sample, the threshold lies below its proportional limit. Data from the loadup portions of other test types (see, e.g., sample 200-18, which was the loadup for a creep test) were also used to increase the number of tensile repeats. Only the loadup portion was plotted, and consequently these tests only attained lower strain and stress magnitudes.

Data for samples tested at 200 °C and various strain rates (Fig. 11) show the typical rate dependency for stress, with slower loading rates yielding lower maximum stresses. The dependence of loading rate on stiffness is apparent by observing the separation of the stress-strain curves at stresses less than 100 MPa. The scatter in threshold stress is also shown as a horizontal grey rectangle and is consistent with the scatter in PL for the two slow-strain-rate ($5 \times 10^{-5} \text{ s}^{-1}$) tensile tests. At 200 °C the proportional limits were higher, but in the range of the threshold stress, Y . By comparing Figure 10 with Figure 11, it was observed that the ultimate strength of GRCop-84 drops over this 180 °C temperature range from 400 to 240 MPa (for equivalent load rate), a decrease of 40 percent.

Another decrease in strength (approximately 15 percent for a similar rate of loading) was observed when the test temperatures were further increased from 200 to 400 °C (Fig. 12). Figure 12 also depicts the decrease in stress with decreasing loading rate. There are two additional tensile curves plotted for samples that were given a “simulated brazing” heat treatment, and both of these are slightly weaker than the as-extruded material. The brazed samples, however, still exhibited the expected rate dependency. Proportional limits were also plotted in this figure for three samples. The PL s were ordered based on strain rates (C201-13, C201-8b, and C200-1) with the slowest rate sample (C201-13) being closest to the threshold region. As expected, they lie slightly above the threshold range calculated using the viscoelastic subtraction technique (Eq. (1)).

At 600 °C a stronger rate dependence on strength was observed (Fig. 13) compared to the lower test temperatures. This can easily be seen by comparing the lower purple curve tested at a rate of $5 \times 10^{-5} \text{ s}^{-1}$ to the upper black curve at a rate of $5 \times 10^{-4} \text{ s}^{-1}$. This one-order-of-magnitude difference in loading rate produced a strength difference of 30 percent (100 vs. 130 MPa). Also note in this graph that the value for the threshold was very low compared to the remainder of the stress-strain curve. The PL for the two tests with the extreme strain rates showed that the PL for the slower rate test fell closer to the threshold than for the faster rate test. In this figure there is also the initial loadup plotted from a creep test at 500 °C, which exhibited slightly stiffer and stronger behavior than the samples tested at 600 °C.

Figure 14 shows the tensile behavior from two samples tested at 800 °C and at a rate of $8.3 \times 10^{-5} \text{ s}^{-1}$. The strengths at this temperature were very low, about 32 percent of the 600 °C strengths and 8 percent of that of the 20 °C tests. Unfortunately, viscoelastic tests to determine the threshold were not conducted at this temperature.

Tensile properties are plotted in Figure 15 as a function of temperature for a loading strain rate of $1 \times 10^{-4} \text{ s}^{-1}$. The average values for the traditional 0.02 and 0.2 percent rate-independent yield definitions $\sigma_{0.02}$ and $\sigma_{0.2}$, respectively (see Hill, 1950; and Chen and Han, 1988), are given as well as individual

sample and mean proportional limits. The viscoelastic threshold stress is also plotted and is the lowest curve in the plot. The difference between the threshold stress and the proportional limit became greater at higher temperatures (see shaded region in Fig. 15). This indicates that contrary to traditional thinking irreversible time-dependent deformation occurs well below the proportional limit and classical yield point definitions. The ultimate tensile strength³ (UTS) is also plotted in this figure. Because of the associated higher stress values a secondary y-axis (see right-hand side of Fig. 15) was employed to denote these strengths.

The tensile behavior of GRCop-84 as a function of temperature is shown in Figure 16. At the test temperatures of 20 and 200 °C the loading rate was $1 \times 10^{-4} \text{ s}^{-1}$, whereas at 400 and 600 °C the loading rate was $5 \times$ higher (i.e., $5 \times 10^{-4} \text{ s}^{-1}$). Except for those at 600 °C these rates were similar enough to have minimal effect on the tensile behavior. Therefore, the effect of temperature on the behavior can easily be observed. Further, it is apparent that brazing will produce a slightly softer (i.e., lower strength) response than that of the as-extruded material. The effects of temperature on the tensile behavior of slow rate tests ($5 \times 10^{-5} \text{ s}^{-1}$) are shown in Figure 17. Clearly, strength decreased with increasing temperature with a significant drop above a temperature of 400 °C. For duplicate tests, the reproducibility was remarkable, particularly at larger strains. There was a large discrepancy between the curves for repeats at 200 and 400 °C in the small-strain (<1-percent) regime, but the curves converged as deformation increased.

One sample (C200-18) was loaded in tension at 20 °C and unloaded after 1-percent strain increments. Three cycles were performed with the final cycle attaining 3-percent axial strain. This test was designed to monitor the modulus change (stiffness degradation; i.e., damage evolution) as a function of load history. Additionally, a second extensometer was added to this test to measure the transverse strain. The results are shown in Figure 18. The tensile behavior for the cyclic test agreed with other tensile tests at similar conditions as observed by comparing a tensile curve from sample C205-12. The loading modulus for each of the three cycles is shown in Figure 18 and indicates a slight decrease with increasing strain cycles. The modulus in this test was lower by 22 percent than the average modulus at 20 °C. The reason for this is unknown. Since all the stress-strain curves were linear up to 140 MPa, the loading moduli for each test was calculated over this stress range, thereby ensuring consistent modulus calculations.

Poisson's ratio was calculated for this test as well and is shown in Figure 19 as a function of axial strain. A reference line is drawn at low strains, which indicates the value of Poisson's ratio (0.402) over the elastic regime. At the proportional limit Poisson's ratio began to increase to a maximum of 0.427 at 1 percent axial strain. During the unloading portion of the cycle, Poisson's ratio increased further to a value of 0.447 and then decreases during reloading. Increasing Poisson's ratio during unloading has also been observed in Ti-6Al-4V (Lerch and Arnold, 2016). Poisson's ratio for GRCop-84 appears to saturate during loading at 0.43 for axial strains greater than 0.01. Values for Poisson's ratio terminated at an axial strain of 0.023 because of saturation of the diametral extensometer signal, and hence the final loading and unloading of the third cycle is not shown in Figure 19. Note that the high value of Poisson's ratio (0.4) was also measured for a second sample (C199-1) loaded only in the linear elastic regime.

Stress Relaxation

Stress relaxation tests were conducted at 200, 400, and 600 °C with a limiting strain of 0.025. A few tests were conducted as well at a lower strain of 0.015. The relaxation behavior of GRCop-84 at 200 °C is shown in Figures 20 and 21. Figure 20 displays the stress-strain curves for two samples loaded at a strain rate of $5 \times 10^{-5} \text{ s}^{-1}$. The first sample (C200-3b) was terminated after 4.2 h because of experimental problems. This test was then repeated using sample C200-14 and run to completion, which included a 24-h relaxation period followed by unloading and a recovery at zero load for 5.2 h.⁴ Figure 20 also shows

³Herein ultimate tensile strength is defined as the maximum stress obtained during a test. This value is typically lower than the real ultimate tensile strength since the samples were not strained that high.

⁴This standard recovery time of 24 h was cut short since it was clear that the strain was never going to return to zero and had nearly reached equilibrium as shown in Figure 21. This sample did recover 160 $\mu\epsilon$ over this time.

the range of the viscoelastic threshold and the proportional limit for each sample. The relaxation behavior (stress vs. time plot) is shown in Figure 21. The stress decreased from 250 to 200 MPa within the first 10 000 s and only slightly decreased thereafter. This saturation limit was over twice the viscoelastic threshold at this temperature. From Figures 20 and 21 it is obvious that significant internal back stress (approximately 125 MPa) due to hardening has accumulated during loading to 2.5 percent strain. Since relaxation within the GVIPS model is driven by the effective stress (difference between the applied stress σ and the internal back stress α (i.e., $\sigma - \alpha$)) the inelastic strain evolution will continue until the applied stress reaches the threshold surface. This surface is defined uniaxially (assuming a J2 formulation) as

$$\alpha = \sigma - Y \quad (3)$$

The contribution of both components to the effective stress is shown in Figure 21. It is observed that the back stress was a significant deformation component at 200 °C. This is in contrast to the work on Ti-6-4 (Lerch and Arnold, 2016) in which samples relaxed to the threshold value between test temperatures of 20 and 538 °C, indicating that the back stress α in that material was zero.

Stress-strain curves for relaxation tests at 400 °C are shown in Figure 22 for two relaxation strains (0.015 and 0.025) and various loading rates. The curves were ranked based on the loading rate with higher stress values occurring for higher loading rates. Also the two “brazed” thermal cycle samples had lower stress values than the as-extruded material. The relaxation curves are shown in Figure 23. The saturation stress occurred at approximately 100 MPa, thus suggesting an internal back stress accumulation of approximately 50 MPa. This clearly suggests that significant thermal annihilation of dislocations is taking place at 400 °C during the relaxation hold period in contrast to the 200 °C behavior. The relaxation curves (Fig. 23) imply that the saturation stress would never reach the threshold value (Y) in any reasonable time. It can be observed in this figure that the lower the strain rate is, the higher the saturation stress is. This lends credence to the earlier statement that not all of the stress was locked in during the slow loading rates. Relaxation at the strain value of 0.015 fell in the middle of the data group yet still exhibits the loading rate behavior discussed earlier. Relaxation at these two strain values suggests that the relaxation behavior was not a strong function of strain in this material. The “brazed” thermal cycle samples also showed equivalent relaxation to the as-extruded material.

The stress-strain behavior for the relaxation tests at 600 °C is shown in Figure 24 for two strain rates. At the faster loading rate, the test was terminated after 17 h because of experimental problems. Therefore, no unload and recovery data were available for this test. For the slower loading rate ($5 \times 10^{-5} \text{ s}^{-1}$) both samples were run to completion, although they were terminated at 16 h into recovery. It is noted in Figure 24 that both of these tests relaxed down to values near the viscoelastic threshold. This is clarified by examining the relaxation curves in Figure 25 and indicated a value for α of approximately zero. This figure also shows that the test with the faster loading rate relaxed to a lower saturation stress than for the slow-rate tests. This is consistent with the earlier discussion on rate dependence during stress relaxation.

Relaxation as a function of temperature is given in Figures 26 and 27 for the two strain levels. In these figures one can easily compare the saturation stress to the threshold values at the various temperatures. Significant thermal recovery was readily observed at 600 °C. As expected, the competitive nature between dislocation motion and pileup (hardening) and thermal annihilation of dislocations (thermal recovery) occurring during high-temperature deformation was enhanced, thus the reason for the smaller and smaller accumulation of internal back stress at the end of the relaxation hold time, at 400 and 600 °C, respectively. Clearly at 600 °C, almost all back stress was removed during the 17-h hold period. This explains why at this temperature the saturation of stress relaxation (zero inelastic strain rate) was coincident with the threshold, Y .

Creep

The stress-strain curves for the creep samples tested at 200 °C are shown in Figure 28 for equivalent elastic loading rates of $1 \times 10^{-4} \text{ s}^{-1}$. The applied creep stress ranged from 69 to 206 MPa. The threshold range is also plotted in this figure. All of these tests were above the threshold and well within the viscoplastic regime. In all cases, the samples were unloaded after a 24-h creep hold and then allowed to recover at zero load. The strain-time behavior is shown in Figure 29 and includes only the earlier portions of recovery. At this temperature, recovery saturated early so the curves were cut off, allowing additional expansion of the x-axis for better clarity. The amount of viscoelastic recovery at this temperature ranged from 38 to 110 $\mu\epsilon$ (compared to 1000 to 6000 $\mu\epsilon$ total accumulation) and increased with increasing creep stress. Figure 30 shows the creep strain as a function of time. Note creep strain is obtained by subtracting the accumulated loading strains up to the applied stress value from the total strain at each subsequent instant in time. It is usually easier to compare among several tests when creep strain is plotted. However, the model requires total axial strain for characterization. Thus both graphs are usually presented. The amount of accumulated creep strain was only 0.0035 for an applied stress of 206 MPa. The associated applied stress was at the sample's $\sigma_{0.2}$ and slightly smaller than the average UTS at 200 °C of 265 MPa. It was also observed that the creep curves at this temperature had a fairly flat secondary regime (low creep rates), indicative of a purely hardening material.

For creep tests at 400 °C the stress-strain curves are shown in Figure 31. The creep stresses ranged from 21 to 172 MPa. The sample tested at 21 MPa was below the viscoelastic threshold and in the viscoelastic regime. All other tests were in the viscoplastic region. Compared to the tests at 200 °C, these samples showed much less nonlinearity during loading but significantly higher secondary creep rates (see Fig. 32). Sample C200-7 at 172 MPa was terminated after 11.7 h because of experimental issues. All other samples were unloaded to zero load and allowed to recover. Again, creep strains as functions of time are plotted in Figure 33. The curve for the viscoelastic test at 21 MPa was indistinguishable from the x-axis, indicating the very small amount of creep exhibited by this sample. The two samples tested at 35 and 69 MPa exhibited identical creep behavior despite their 2 \times difference in applied load. The higher stressed sample (C201-9b) slightly exceeded its proportional limit during loading, whereas the lower stressed sample (C201-18) did not. We believe that the small amount of plasticity reduced the amount of creep exhibited by the higher stressed sample. Creep at the highest stress of 172 MPa showed a substantial amount of accumulated creep strain (1.5 percent). This was significantly higher than what was observed at 200 °C at all stress levels (see Fig. 30 for comparison). This sample was loaded above its $\sigma_{0.2}$ and slightly below the average UTS of 207 MPa at 400 °C. All of the other creep samples at this temperature exhibited smaller strains, similar to those observed at 200 °C.

Stress-strain curves for creep tests at 600 °C are shown in Figure 34 along with the one curve for a test at 500 °C. Applied stresses were 34, 51, and 69 MPa for the 600 °C tests and 109 MPa for the 500 °C test. The lowest stress sample (C199-16) was above the viscoelastic threshold, but below its proportional limit. All other samples were tested at stress levels at or above their $\sigma_{0.02}$. Most of the loadups appeared linear, indicating that little viscoplastic behavior was incurred during the relatively fast loadup. Note also that the lowest stress sample was tested at a slightly lower loading rate of $2.8 \times 10^{-5} \text{ s}^{-1}$. All samples were unloaded for recovery at zero load, except sample C200-19, which broke after 11 h. Total strain-time plots are shown in Figure 35 and indicate that three out of the four tested samples crept into the tertiary regime. The lowest stressed sample only experienced primary and secondary creep. Creep strains are given in Figure 36. Since the loadup portion is predominantly linear, Figures 35 and 36 appear very similar. They also show that the accumulated creep strains are very much larger than what occurs at the other, lower test temperatures, except for sample C199-16, which was subjected to a very low creep stress.

The next series of plots indicates the effect of temperature on creep at a given stress level. The lowest stress level was 34 MPa, and the curves for these tests are shown in Figures 37 to 39. At this stress, samples were tested at 200, 400, and 600 °C, with more creep occurring as temperature increases. For the test at 200 °C, the stress was below the viscoelastic threshold; this is more easily observed in Figure 38

where the maximum reversible strain limits ($\epsilon_{\max}^R = Y/E_S$) for each temperature are given. It can be again observed in Figure 38 that the sample tested at 200 °C recovered to zero strain during recovery (i.e., all deformation was reversible), whereas the final strain for the other two samples remains well above zero (deformation is predominantly irreversible). The creep strains are shown in Figure 39. A large amount of creep was observed at 600 °C compared to very little at the other two temperatures.

Figures 40 to 42 show the creep results for stress levels of 69 MPa. The stress-strain curves in Figure 40 indicated that all of the tests were at stresses above the threshold. Note that the test at 600 °C experienced strains larger than 0.4 percent, but the data were terminated in this figure to expand the x-axis for easier viewing. The samples at the two lower temperatures were loaded past their proportional limits. At 600 °C the sample was loaded past the $\sigma_{0.02}$. The amount of strain incurred at 600 °C (Figs. 41 and 42) was very large (8 percent) and dwarfs the strain at the other two temperatures. The 600 °C sample broke after 11 h. Consequently, the y-axis was amplified by approximately a factor of 20 in Figure 42 to enhance clarity; thus only a small portion of the 600 °C curve is shown.

At a creep stress of 103 MPa two samples were tested: one at 400 °C and one at 500 °C. At this stress, an increase of 100 °C made a huge difference in the accrued creep, as shown in Figure 43. This drop off in stress-carrying capability was supported by the drop off in the viscoelastic threshold as shown in Figure 9. The range of the threshold at 400 °C is also shown in Figure 43, and the creep stress was far above this level. Both samples exceeded their $\sigma_{0.02}$ during loadup. They were both unloaded and recovered (Fig. 44). The sample tested at 500 °C crept into the tertiary regime with 4.3 percent accumulated creep strain (Fig. 45), but was unloaded before it broke. Note that there is no test shown for 600 °C because the stress is at the UTS of the material at 600 °C. Hence, the remainder of the creep plots will not contain 600 °C data.

Figures 46 to 48 present the creep behavior at 137 MPa for two samples at 200 °C and one at 400 °C. All three samples were loaded past their respective $\sigma_{0.02}$. While the two samples at 200 °C were crept at the same stress, sample C200-15 exhibits slightly more nonlinearity during loadup, and this was probably a reflection of its slightly lower yield point. It likely also exhibited more creep strain (Figs. 47 and 48) for the same reason. Threshold ranges for both temperatures are also shown in Figures 46 and 47.

One sample each was tested at 172 MPa and both 200 and 400 °C, and their behavior is shown in Figures 49 to 51. The 200 °C sample was loaded past its $\sigma_{0.02}$, whereas the 400 °C sample was loaded past its $\sigma_{0.2}$. There was limited creep (0.0008) at the lower temperature. The sample tested at 400 °C tripped a strain limit, but had already accumulated a creep strain of 0.015. Comparisons to the temperature-dependent thresholds are presented in Figures 49 and 50.

Table IV lists some creep attributes for the various tests. Creep stress is given along with the minimum creep rate. The highlighted samples are from tensile tests where the loading rate is given as the minimum creep rate, and the stress is the UTS. Time to percent creep strain is also listed in this table. Note that most of the tests only crept to small strains, particularly for those in the viscoelastic regime. Time to creep strain (i.e., 0.01, 0.05, 0.1, and 0.2 percent) is plotted versus stress in Figure 52. Linear fits are given for the three main temperatures and creep strains of 0.01 percent, where more data were collected. As expected, the slope of these fits becomes steeper with increasing temperatures since the material creeps more readily and has a higher stress dependence.

The applied creep stress is plotted as a function of the minimum creep rate in Figure 53. The data indicate a multilinear behavior at lower temperatures. We would expect the material to exhibit similar behavior at 600 °C if lower creep stresses had been used, consistent with what was observed in Ti-6-4 at the highest temperatures (Lerch and Arnold, 2016). The values for the tensile tests indicated in Table IV are also plotted and represent the data at the highest creep rates. Least squares regression fits at the high stress levels tend to extrapolate to much lower creep rates (to approximately 10^{-8} s^{-1}) and have high creep exponents, n , where $1/n$ is the slope of the curve. The lowest stresses for GRCop-84 at 200 and 400 °C were all from viscoelastic tests and therefore were not expected to show much change in creep rate with changing stress. It was shown for Ti-6Al-4V that the data for the viscoelastic tests fell on a third line in

this plot with a stress exponent of 1.6 (Lerch and Arnold, 2016), which is similar to the creep exponent of 0.8 for the viscoelastic GRCo-84 data at 400 °C (Fig. 53). The solid lines in Figure 53 were taken from values given in Ellis, Carter, and Ferry (2015). Their fits agree well with the data points from this study for similar temperatures.

Estimates of the creep activation energy are given in Figure 54. The activation energies are calculated from the fits of the dotted lines, which were taken from Ellis, Carter, and Ferry (2015) for extruded GRCo-84. These fits agree with the data points from this study at temperatures above approximately 450 °C. At temperatures below this the data show that the slope is much shallower, yielding an activation energy of only 53 kJ/mol. In contrast, the activation energy is approximately 250 and 350 kJ/mol at the higher temperatures and is stress dependent. Both of these values are higher than the reported value for core diffusion in pure copper and was suggested by Ellis, Carter, and Ferry (2015) to be a result of the Cr₂Nb precipitates in the GRCo-84, which result in hindering dislocation movement and increasing the creep resistance.

Discussion

This study documents the time-dependent behavior of the high-temperature copper alloy GRCo-84. Time-dependent deformation in this alloy was found to be both reversible and irreversible. At low applied stresses the deformation was fully reversible and exhibit similar features to the viscoelastic behavior observed in titanium alloys (Lerch and Arnold, 2014; Saleeb and Arnold, 2001; and Arnold, Saleeb, and Castelli, 2001). An upper bound was calculated for the extent of this behavior, and this value is the viscoelastic threshold Y as described by Arnold, Saleeb, and Castelli (2001). Above this threshold deformation was only partially reversible, with the bulk being irreversible, which in turn left permanent offsets after unloading. Although the viscoelastic characterization is probably only applicable to the model described by Saleeb and Arnold (2001) and Arnold, Saleeb, and Castelli (2001), the higher stress, viscoplastic data can certainly be used by any formulation that models time dependency. Moreover, these data can be used for preliminary design of GRCo-84 components. This is probably the most complete study of time dependency for this alloy and the best available data set for design purposes.

GRCo-84 exhibits rate-dependent tensile behavior as shown in Figures 10 to 13. The material strength decreases with increasing temperature at any given loading rate as shown in Figures 15 to 17. A 92-percent decrease in UTS was observed between 20 and 800 °C (Fig. 15).

Stress relaxation was observed at 200 °C and above. Although not investigated, we suspect that some stress relaxation will also occur at lower temperatures, even at room temperature, although with much smaller amounts and over much longer times. At 200 °C, the stress relaxed at least 50 MPa over a 24-h period. This amount was observed for a slow loading rate of $5 \times 10^{-5} \text{ s}^{-1}$. For faster rates, we expect more rapid relaxation to occur, since it will have less time to dissipate during the loading process. The saturation stress at 200 °C (and 400 °C) was higher than the viscoelastic threshold, the difference being attributed to the accumulation of internal (or back) stress as expressed in Equation (3). At these temperatures the hardening (i.e., back stress) is significant. At 600 °C the relaxation amount was 100 MPa and saturated near the viscoelastic threshold even at the slower strain rates. This indicates that there is very little, if any, back stress remaining. This is similar to what was observed by Lerch and Arnold (2016) for Ti-6Al-4V. For that material it was found that relaxation always saturated at the threshold implying a back stress of zero over the entire temperature range studied.

Limited data for GRCo-84 also suggests that the relaxation strain (i.e., target strain) does not play a significant role in the amount of subsequent relaxation that occurs (Fig. 23). This is because all hardening has already taken place (at relatively low strain as compared with the target values investigated).

Significant amounts of creep can also be accrued within 24 h in this alloy. Even at 200 °C, creep strains of 0.35 percent are observed for stresses on the order of the $\sigma_{0.2}$. At higher temperatures, creep strains over 1 percent are attainable for stresses at the yield point (400 °C), and 8-percent accumulation and sample failure occur at 600 °C. A 1-percent creep strain in 24 h would require stresses close to the

UTS at 200 °C, the $\sigma_{0.2}$ at 400 and 500 °C, and between the $\sigma_{0.02}$ and $\sigma_{0.2}$ at 600 °C. For the stresses used in this study, tertiary creep was only observed at temperatures above 400 °C.

Taken together, these results indicate that GRCo-84 will undergo significant time-dependent deformations even near room temperature. Given that the base of the alloy is copper, a relatively weak but very ductile metal, this is not too surprising. Depending upon the application, these time-dependent changes in strain may be significant. While a fraction of a percent change in the throat profile of a rocket engine liner may not produce a change in thrust, it could develop or relieve thermally induced stresses in that section, shortening or lengthening the life of the liner. Likewise, applications with tight tolerances may require time-dependent analyses if they are loaded or subject to thermally induced stresses. Bolted parts may deform with time and lose their required clamping force. This has implication for the inspection and maintenance of the liner, injector, and other parts made from GRCo-84.

Conclusions

1. GRCo-84 exhibits time-dependent reversible and irreversible behavior at temperatures of 20 °C and above with substantial viscoplastic behavior above 400 °C.
2. GRCo-84 exhibits an explicit threshold value delineating reversible from irreversible deformation. The viscoelastic threshold, Y , is referenced to the various load levels in these tests.
3. Utilizing traditional “plastic” definitions of yield most likely will result in nonconservative designs.
4. Both the viscoelastic and viscoplastic behavior of GRCo-84 is consistent with that observed in titanium- and nickel-base alloys and is well described by the GVIPS model.
5. The time- and rate-dependent behaviors of GRCo-84 are important when considering applications such as reusable launch vehicles and have implication relative to their proper inspection and preventative maintenance protocols.

References

- Arnold, S.M.; Saleeb, A.F.; and Castelli, M.G., 2001: A General Time Dependent Constitutive Model: Part II—Application to a Titanium Alloy. *J. Eng. Mater. Technol. Trans.*, vol. 123, pp. 65–73.
- Arnold, Steven M., et al., 2009: An Overview of Prognosis Health Management Research at Glenn Research Center for Gas Turbine Engine Structures With Special Emphasis on Deformation and Damage Modeling. NASA/TM—2009-215827. <http://ntrs.nasa.gov>
- Arnold, Steven M.; Lerch, Bradley A.; and Sellers, Cory, 2013: Experimental Identification and Simulation of Time and/or Rate Dependent Reversible and Irreversible Deformation Regions for Both a Titanium and Nickel Alloy. Presented at the International Symposium on Plasticity and Its Current Applications, Nassau, Bahamas.
- Arnold, Steven M., et al., 2013: Viscoelastoplastic Deformation and Damage Response of Titanium Alloy, Ti-6Al-4V, at Elevated Temperatures. Presented at the International Symposium on Plasticity and Its Current Applications, Nassau, Bahamas.
- Arnold, Steven M., et al. 2014: Viscoelastoplastic Deformation and Damage Response of a Titanium (Ti-6-4) and Nickel-based Superalloy (ME3) at Elevated Temperatures. Presented at the 2014 SEM Annual Conference and Exposition on Experimental and Applied Mechanics, Greenville, SC.
- ASTM Standard E1876–15, 2009: Standard Test Method for Dynamic Young’s Modulus, Shear Modulus, and Poisson’s Ratio by Impulse Excitation of Vibration. ASTM International, West Conshohocken, PA.
- Chen, Wai Fah; and Han D.J., 1988: *Plasticity for Structural Engineers*. Springer-Verlag, New York, NY.
- de Groh III, Henry C.; Ellis, David L.; and Loewenthal, William S., 2007: Comparison of GRCo-84 to Other High Thermal Conductive Cu Alloys. NASA/TM—2007-214663. <http://ntrs.nasa.gov>
- Ellis, D., 2002: GRCo-84. Aerospace Structural Materials Database (ASMD), Version 6.1. CINDAS LLC, West Lafayette, IN. <http://www.cindasdata.com/> Accessed Feb. 16, 2017.

- Ellis, D.L.; Carter, J.L.W.; and Ferry, M.H., 2015: A Statistical Study of the Effects of Processing Upon the Creep Properties of GRCop-84. *Mat. Sci. Eng. A-Struct.*, vol. 640, no. 29, pp. 1–15.
- Ellis, David L., 2005: GRCop-84: A High-Temperature Copper Alloy for High-Heat Flux Applications. NASA/CR—2005-213566. <http://ntrs.nasa.gov>
- Ellis, David L.; and Hastings, Keith, 2006: Effects of Hydrogen on GRCop-84. NASA/TM—2006-214269. <http://ntrs.nasa.gov>
- Ellis, David L.; and Michal, Gary M., 1989: Precipitation Strengthened High Strength, High Conductivity Cu-Cr-Nb Alloys Produced by Chill Block Melt Spinning, NASA/CR—1989-185144. <http://ntrs.nasa.gov>
- Ellis, David L.; and Michal, Gary M., 1996: Mechanical and Thermal Properties of Two Cu-Cr-Nb Alloys and NARloy-Z. NASA CR—198529. <http://ntrs.nasa.gov>
- Ellis, David L.; Keller, Dennis J.; and Nathal, Michael, 2000: Thermophysical Properties of GRCop-84. NASA/CR—2000-210055. <http://ntrs.nasa.gov>
- Ellis, David L.; Loewenthal, William S.; and Yun, Hee Man, 2012: Tensile Properties of GRCop-84. NASA/TM—2012-217108. <http://ntrs.nasa.gov>
- Hill, Rodney, 1950: *The Mathematical Theory of Plasticity*. Clarendon Press, Oxford.
- Ibrahimbegovic, Adnan, 2009: *Nonlinear Solid Mechanics: Theoretical Formulations and Finite Element Solution Methods*. Springer Science & Business Media, New York, NY, p. 186.
- Lerch, B.A.; and Arnold, S.M., 2014: Viscoelastic Response of the Titanium Alloy Ti-6-4: Experimental Identification of Time- and Rate-Dependent Reversible and Irreversible Deformation Regions. NASA/ TM—2014-216584.
- Lerch, Bradley A.; and Arnold, Steven M., 2016: Viscoplastic Characterization of Ti-6Al-4V: Experiments. NASA/TM—2016-218864. <http://ntrs.nasa.gov>
- Loewenthal, William S.; and Ellis, David L., 2008: GRCop-84 Rolling Parameter Study. NASA/TM—2008-215213. <http://ntrs.nasa.gov>
- Loewenthal, William S.; and Ellis, David L., 2011: Sources of Variation in Creep Testing. NASA/TM—2011-215493. <http://ntrs.nasa.gov>
- Raj, S.V., et al., 2006: Cyclic Oxidation Behavior of Cold Sprayed CuCrAl-Coated and Uncoated GRCop-84 Substrates for Space Launch Vehicles. NASA/TM—2006-214350. <http://ntrs.nasa.gov>
- Saleeb, A.F.; and Arnold, S.M., 2001: A General Time Dependent Constitutive Model: Part I—Theoretical Developments. *J. Eng. Mater. Technol. Trans.*, vol. 123, pp. 51–64.
- Saleeb, A.F.; and Arnold, S.M., 2004: Specific Hardening Function Definition and Characterization of a Multimechanism Generalized Potential-Based Viscoelastoplasticity Model. *Int. J. Plasticity*, vol. 20, pp. 2111–2142.
- Saleeb, A.F., et al., 2001: A General Hereditary Multimechanism-Based Deformation Model With Application to the Viscoelastoplastic Response of Titanium Alloys. *Int. J. Plasticity*, vol. 17, pp. 1305–1350.
- Sinha, N.K., 2001: Short Strain Relaxation/Recovery Tests for Evaluating Creep Response of Nickel-Base Superalloys Like IN-738LC. *J. Mater. Sci. Lett.*, vol. 20, pp. 951–953.
- Sinha, Nirmal K., 2005: Short-Term Rheology of a Polycrystalline Nickel-Base Superalloy Involving Delayed Elasticity. *ECCC Creep Conference*, London, pp. 256–267.
- Thomas-Ogbuji, Linus U.; and Humphrey, Donald L., 2000: Oxidation Behavior of GRCop-84 (Cu-8Cr-4Nb) at Intermediate and High Temperatures. NASA/CR—2000-210369. <http://ntrs.nasa.gov>

TABLE I.—AVERAGE CHEMISTRY OF GRCop-84 EXTRUSION

Cr		Nb		Cr:Nb ratio		Cr+Nb		Cr ₂ Nb (calculated)	Fe	Mn	O	Si	Cu
wt%	at. %	wt%	at. %	wt%	at. %	wt%	at. %	vol%	ppm	ppm	ppm	ppm	
6.58	8.11	5.78	3.97	1.14	2.04	12.39	12.08	14.22	167	0	414	0	Bal.

TABLE II.—TEST MATRIX FOR CHARACTERIZATION OF GRCop-84

Sample ^a	Test type	Level	Strain rate, s ⁻¹	Modulus, <i>E</i> , GPa	Proportional limit, <i>PL</i> , MPa	0.02% yield stress, $\sigma_{0.02}$, MPa	0.2% yield stress, $\sigma_{0.2}$, MPa	Comments ^b
20 °C								
C199-1	Modulus	±0.01	1×10 ⁻⁴	115				Poisson's ratio measurements
C200-18	Creep	7 MPa	1×10 ⁻⁴	105				Below <i>Y</i>
C200-11	Creep	7 MPa	1×10 ⁻⁴	104				Below <i>Y</i>
C200-18	Cyclic Tension	3.0%	1×10 ⁻⁴	83	102.6	124.6	171.3	3 cycles
200 °C								
C200-3 ^c	Creep	7 MPa	9×10 ⁻⁵	55				Below <i>Y</i>
C200-12	Creep	7 MPa	1×10 ⁻⁴	97	56.9			Below <i>Y</i>
C200-12	Creep	14 MPa	1×10 ⁻⁴	97				Below <i>Y</i>
C200-12	Creep	34 MPa	1×10 ⁻⁴	97				Below <i>Y</i>
C200-12	Creep	69 MPa	1×10 ⁻⁴	97				Above yield
C200-12	Creep	137 MPa	1×10 ⁻⁴	97	82.7	118.2		Above yield
C200-15	Creep	137 MPa	1×10 ⁻⁴	93	56.9	106.6		Above yield
C200-8	Creep	172 MPa	1×10 ⁻⁴	94	49.0	115.3		Above yield
C200-2	Creep	206 MPa	1×10 ⁻⁴	98	70.4	118.4	202.1	Above yield
C200-3b	Relaxation	2.5%	5×10 ⁻⁵	70	53.4	84.3	175.7	Control problems
C200-14	Relaxation	2.5%	5×10 ⁻⁵	87	76.1	115.5	195.4	Above yield
400 °C								
C201-12	Modulus	±0.01%	0.001– 1×10 ⁻⁵					RT,200,300,400,500,600 °C
C201-6	Modulus	±0.02%	0.001– 1×10 ⁻⁵					RT,200,300,400,500,600 °C
C201-17	Relaxation	0.004%	8×10 ⁻⁵					Control error
C201-9	Relaxation	0.02%	1×10 ⁻⁴	71				Below <i>Y</i>
C201-9a	Relaxation	0.04%	1.1×10 ⁻⁴	76				Above <i>Y</i>
C201-15	Creep	4 MPa	8×10 ⁻⁵	--				Below <i>Y</i>
C201-1	Creep	14 MPa	1×10 ⁻⁴	71				Below <i>Y</i>
C201-20(B)	Creep	14 MPa	1×10 ⁻⁴	75				Below <i>Y</i>
C201-19a	Creep	21 MPa	1.1×10 ⁻⁴	80				Below <i>Y</i>
C201-8(B)	Creep	21 MPa	1.1×10 ⁻⁴	69				Below <i>Y</i>
C201-18	Creep	35 MPa	1×10 ⁻⁴	76				Above <i>Y</i>
C201-9b	Creep	69 MPa	1×10 ⁻⁴	74	61.4			With 2 prior threshold tests
C201-19b	Creep	103 MPa	1×10 ⁻⁴	77	59.9	88.2		Above yield
C200-20	Creep	137 MPa	1×10 ⁻⁴	82	58.9	97.1		Above yield
C200-7	Creep	172 MPa	1×10 ⁻⁴	86	47.9	90.2	169.5	Above yield
C201-15b	Relaxation	1.5%	5×10 ⁻⁴	73	74.8	84.6	158.8	Above yield
C201-17b	Relaxation	1.5%	5×10 ⁻⁵	71	65.3	74.3	138.7	Above yield
C201-4	Relaxation	2.5%	4.9×10 ⁻⁵	84	96.5	106.2	166.1	Mode switch error
C201-13	Relaxation	2.5%	3×10 ⁻⁶	74	53.7	80.0	154.7	Above yield
C201-8b(B)	Relaxation	2.5%	6.1×10 ⁻⁶	62	60.2	67.4	134.5	Above yield
C201-20b(B)	Relaxation	2.5%	5×10 ⁻⁴	75	58.8	83.0	144.8	Control problems
C201-1b	Relaxation	2.5%	5×10 ⁻⁴	83	74.4	93.7	161.5	Above yield
C200-1	Relaxation	2.5%	5×10 ⁻⁴	90	79.9	109.7	177.3	Above yield
C201-11	Relaxation	2.5%	6×10 ⁻⁶	80	51.7	79.4	156.0	Above yield
C200-11	Relaxation	2.5%	5×10 ⁻⁵	85	52.5	83.9	153.3	Above yield

TABLE II.—Concluded.

Sample ^a	Test type	Level	Strain rate, s ⁻¹	Modulus, <i>E</i> , GPa	Proportional limit, <i>PL</i> , MPa	0.02% yield stress, $\sigma_{0.02}$, MPa	0.2% yield stress, $\sigma_{0.2}$, MPa	Comments ^b
500 °C								
C199-8	creep	109 MPa	1×10^{-4}	75	58.8	88.1		above yield
600 °C								
C199-16	creep	34 MPa	2.8×10^{-5}	63				below yield
C199-11	creep	51 MPa	1×10^{-4}	67	35.5	51.5		below yield
C200-19	creep	69 MPa	1×10^{-4}	61	39.2	61.6		below yield
C199-1	relaxation	1.5%	5×10^{-5}	62	45.3	53.5	87.3	above yield
C199-10	relaxation	2.5%	5×10^{-5}	66	33.0	53.5	88.0	above yield
C199-20	relaxation	2.5%	5×10^{-4}	71	62.9	82.5	119.4	above yield
800 °C								
193-8	tensile	22%	8.3×10^{-5}	22	18.5	21.1	22.5	powder lot 3
202-12	tensile	22%	8.3×10^{-5}	33	16.2	17.9	25.9	powder lot 3

^a(B) denotes simulated brazing treatment.^bY is threshold stress, and RT is room temperature.^cPoor strain resolution.

TABLE III.—TENSILE AND VISCOELASTIC PROPERTIES FOR GRCop-84

Test temperature, °C	Sample	Tensile				Viscoelastic ^a		
		Modulus, <i>E</i> , GPa	Proportional limit, <i>PL</i> , MPa	0.02% yield stress, $\sigma_{0.02}$, MPa	0.2% yield stress, $\sigma_{0.2}$, MPa	Infinitely slow modulus, <i>E_s</i> , GPa	Threshold stress, <i>Y</i> , MPa	<i>Y/PL</i>
extruded								
20	C200-18	105.0	102.6	124.6	231.0	105.0	102.6	1.00
200	C200-15	93.2	56.9	106.6		90.6	59.5	1.04
200	C200-12	97.2	82.7	118.2		90.6	84.5	1.02
400	C201-9b	73.9	61.5			58.3	52.1	0.85
400	C201-18	75.7	62.8			58.3	15.9	0.25
500	C199-8	74.5	58.8	88.1		39.3	20.7	0.35
600	C199-16	63.2				6.7	7.7	0.16
800	193-8	22.1	18.5	21.1	34.6			
800	202-12	32.7	16.2	17.9	25.9			

^aValues in shaded cells are estimated.

TABLE IV.—CREEP PROPERTIES FOR GRCop-84

Sample	Creep stress, MPa	Minimum creep rate, s ⁻¹	Time to percent creep strain, s						
			0.01	0.05	0.10	0.20	0.50	1.00	Tertiary
200 °C									
C200-3	7.2	4.0×10 ⁻¹⁰	63 479						
C200-12	13.7	8.4×10 ⁻¹⁰	68 160						
C200-12	34.3	2.9×10 ⁻¹⁰							
C200-12	68.7								
C200-12	137.3	3.1×10 ⁻¹⁰	270						
C200-15	137.3		54						
C200-8	171.7	8.3×10 ⁻¹⁰	7	850					
C200-2	206.1	3.9×10 ⁻⁹	1	16	62	780			
C196-12	287.0	8.3×10 ⁻⁵							
C200-3b	260.0	5.0×10 ⁻⁵							
400 °C									
C201-15	3.8	9.4×10 ⁻¹¹	16 679						
C201-1	14.0	7.4×10 ⁻¹⁰	47 040						
C201-20	14.2	2.3×10 ⁻⁹	90 000						
C201-19a	20.8	9.9×10 ⁻¹¹	48 298						
C201-8	21.4	1.2×10 ⁻⁹	50 000						
C201-18	34.9	1.1×10 ⁻⁹	8 400						
C201-9b	69.2	1.8×10 ⁻⁹	9 000						
C201-19b	103.4	6.6×10 ⁻⁹	51	10 320	54 120				
C200-20	137.4	1.6×10 ⁻⁸	10	600	4 380	26 400			
C200-7	171.7	2.5×10 ⁻⁷	2	22	111	720	6040	22 290	
C200-18	230.0	8.3×10 ⁻⁵							
C200-1	230.0	5.0×10 ⁻⁴							
C200-11	210.0	5.0×10 ⁻⁵							
500 °C									
C199-8	108.5	3.8×10 ⁻⁷	4	54	195	820	5280	17 350	39 720
600 °C									
C199-16	34.3	2.5×10 ⁻⁸	31	330	2 040	11 280			
C199-11	51.4	4.5×10 ⁻⁷	4	33	130	640	5020	15 840	31 200
C200-19	68.6	1.4×10 ⁻⁶	1	20	65	245	1520	4 930	13 200
C194-12	115.0	8.3×10 ⁻⁵							
C199-20	130.0	5.0×10 ⁻⁴							
C199-10	105.0	5.0×10 ⁻⁵							

^aHighlighted rows are values from tensile tests.

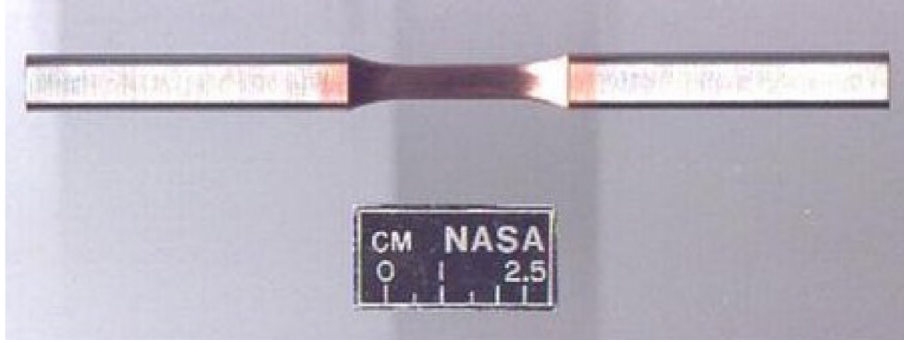


Figure 1.—GRCop-84 test sample with stainless steel ends.

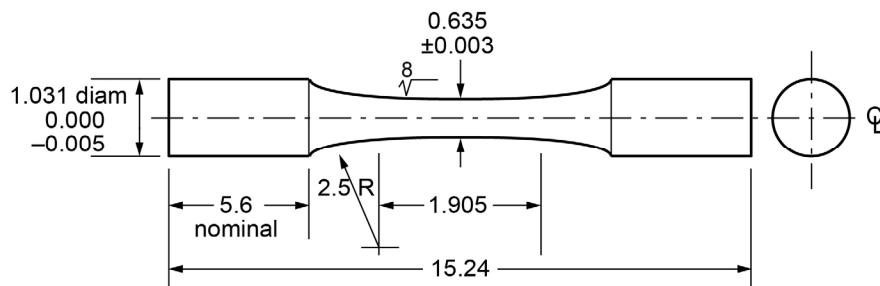


Figure 2.—Test sample (dimensions in centimeters).

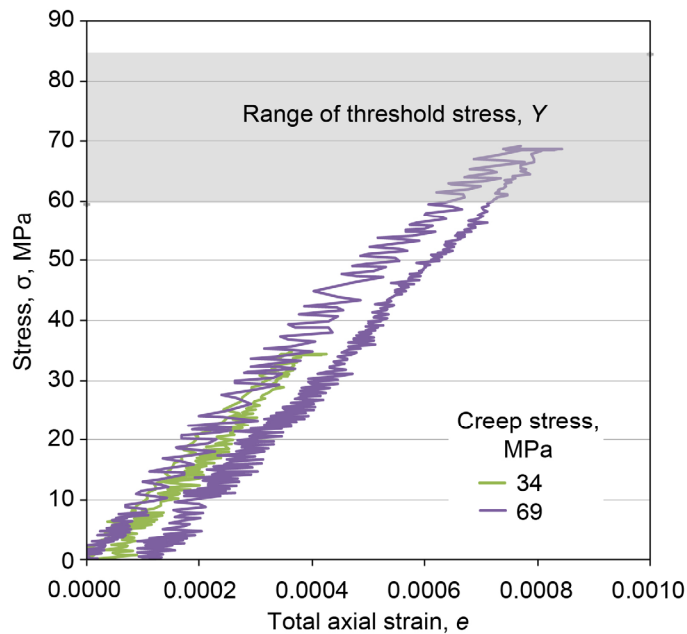


Figure 3.—Stress-strain curves of GRCop-84 (sample C200-12) for viscoelastic tests at 200 °C and strain rate of 0.0001 s^{-1} , showing range of threshold stress Y .

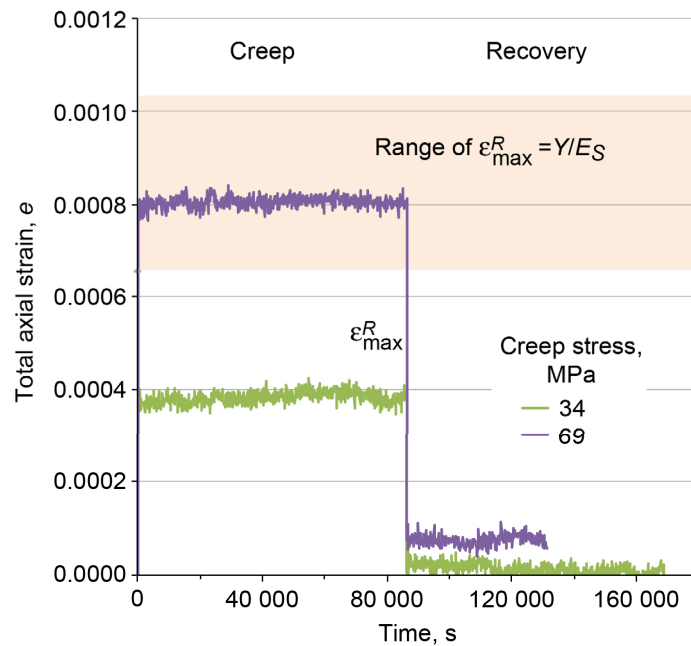


Figure 4.—Strain-time response of GRCop-84 (sample C200-12) for viscoelastic tests at 200 °C and strain rate of 0.0001 s^{-1} , showing range of maximum reversible strain ϵ_{\max}^R , where Y is threshold stress and E_S is infinitely slow modulus.

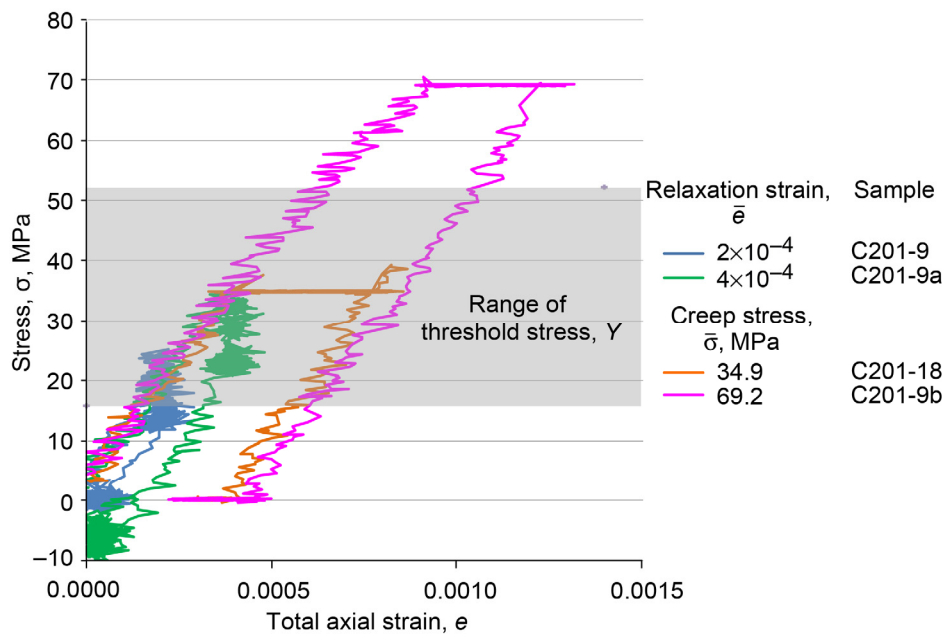


Figure 5.—Stress-strain curves of GRCop-84 for viscoelastic tests at 400 °C and strain rate of 0.0001 s^{-1} , showing range of threshold stress Y .

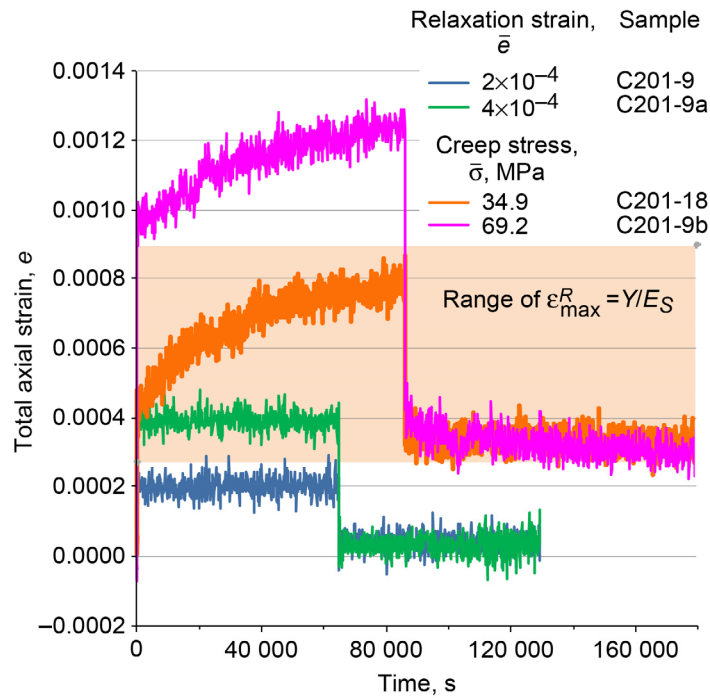


Figure 6.—Strain-time response of GRCop-84 for viscoelastic tests at 400 °C and strain rate of 0.0001 s^{-1} , where ϵ_{\max}^R is maximum reversible strain, Y is threshold stress, and E_S is infinitely slow modulus.

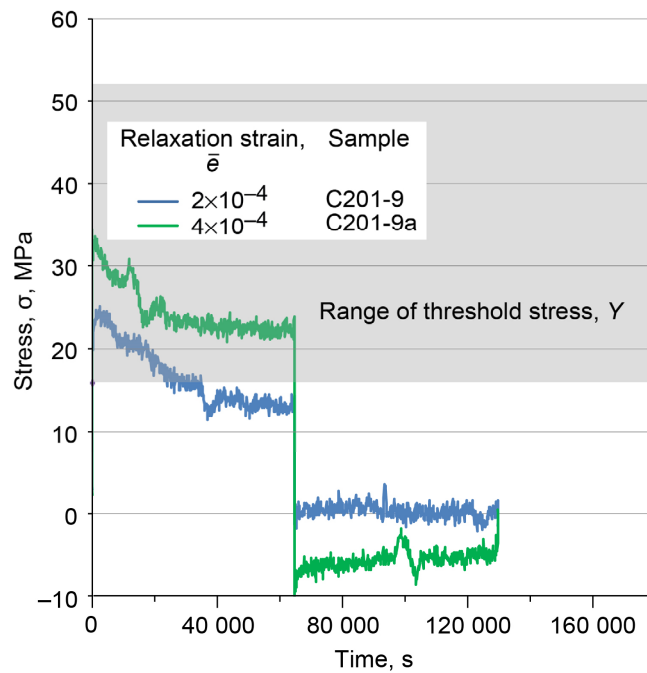


Figure 7.—Stress relaxation of GRCop-84 followed by unloading and recovery at 400 °C, showing range of threshold stress Y .

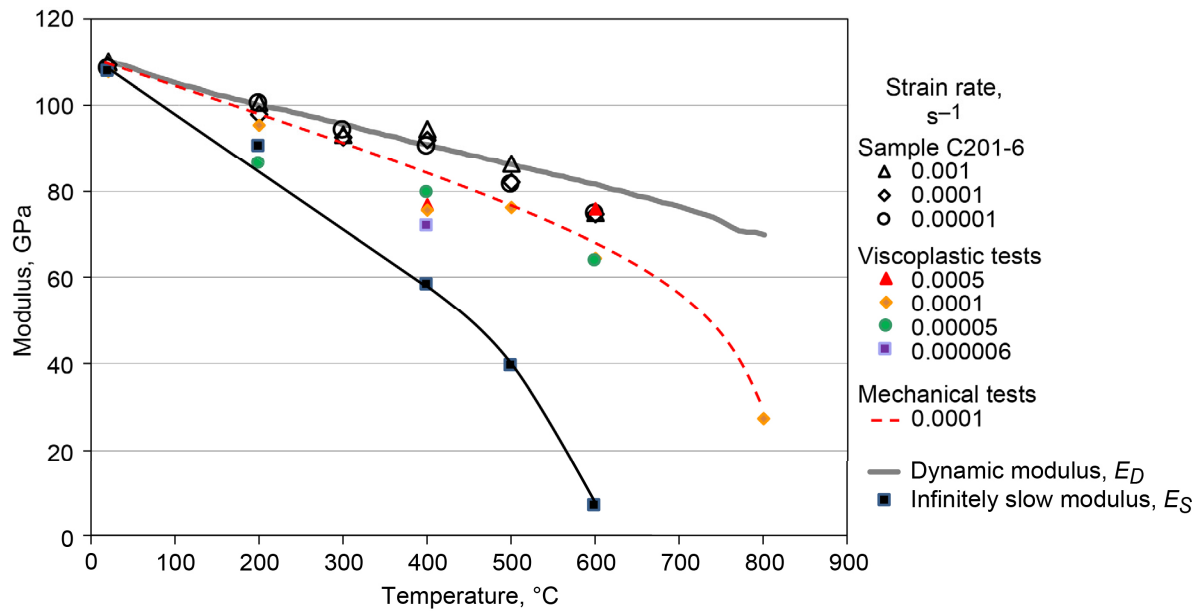


Figure 8.—Modulus for GRCop-84 as function of temperature and strain rate.

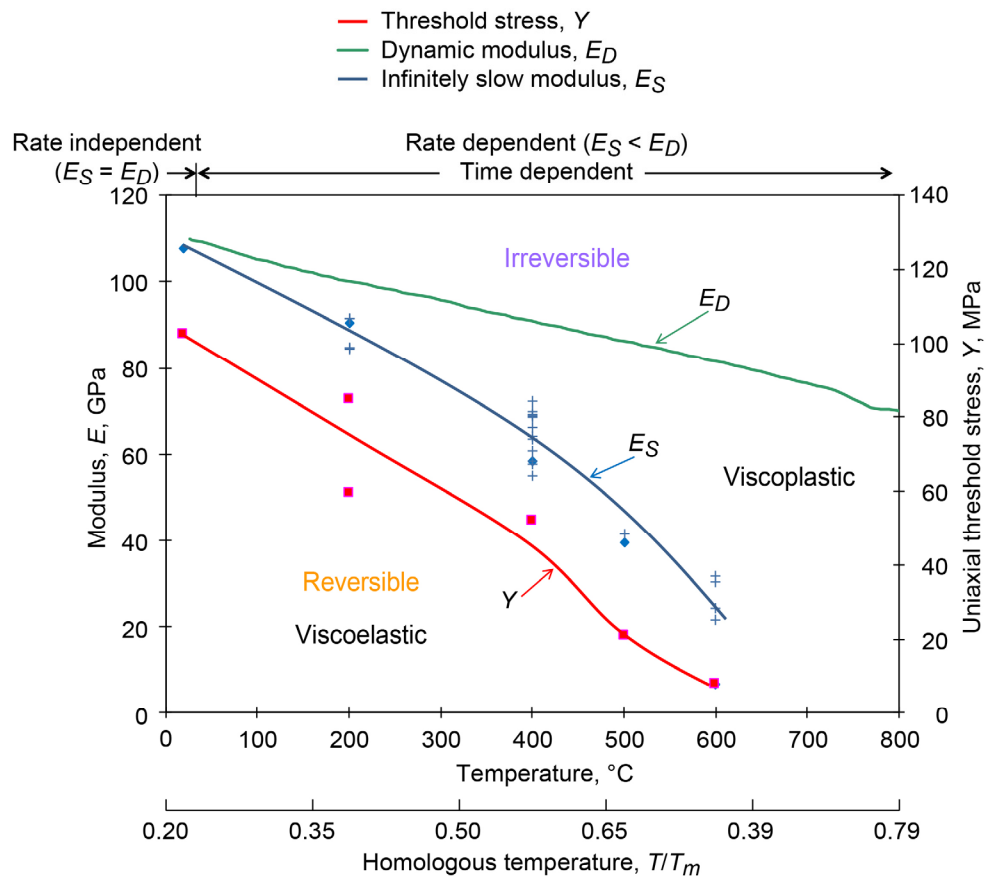


Figure 9.—GRCop-84 time-dependent deformation modeling map, where T and T_m are the test temperature and melting temperature, respectively.

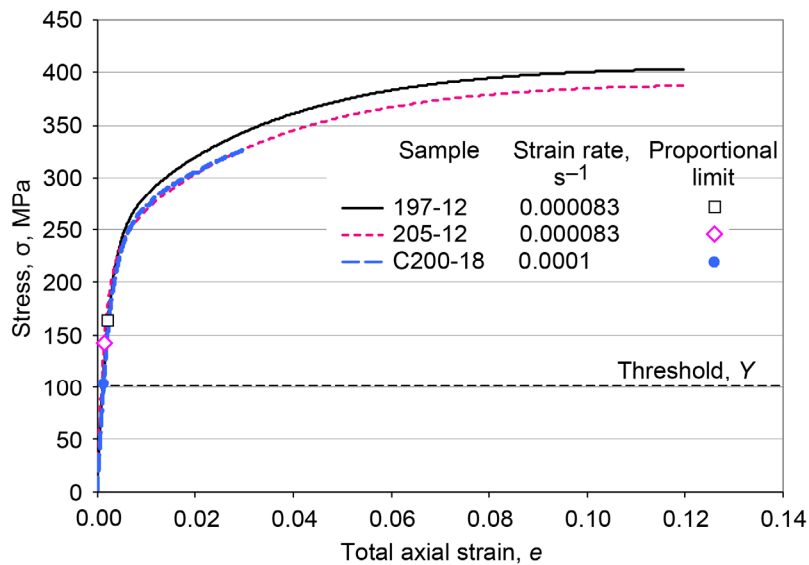


Figure 10.—Tensile stress-strain curves for GRCop-84 at 20 °C and strain rate of $0.0001\ s^{-1}$, showing threshold stress Y and proportional limits PL .

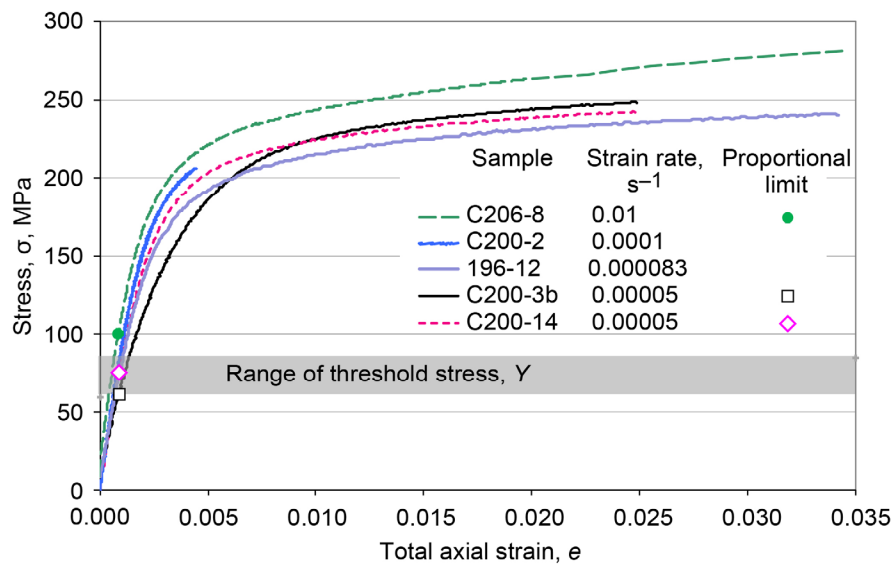


Figure 11.—Tensile stress-strain curves for GRCop-84 at 200 °C and different strain rates, showing range of threshold stress Y and proportional limits PL .

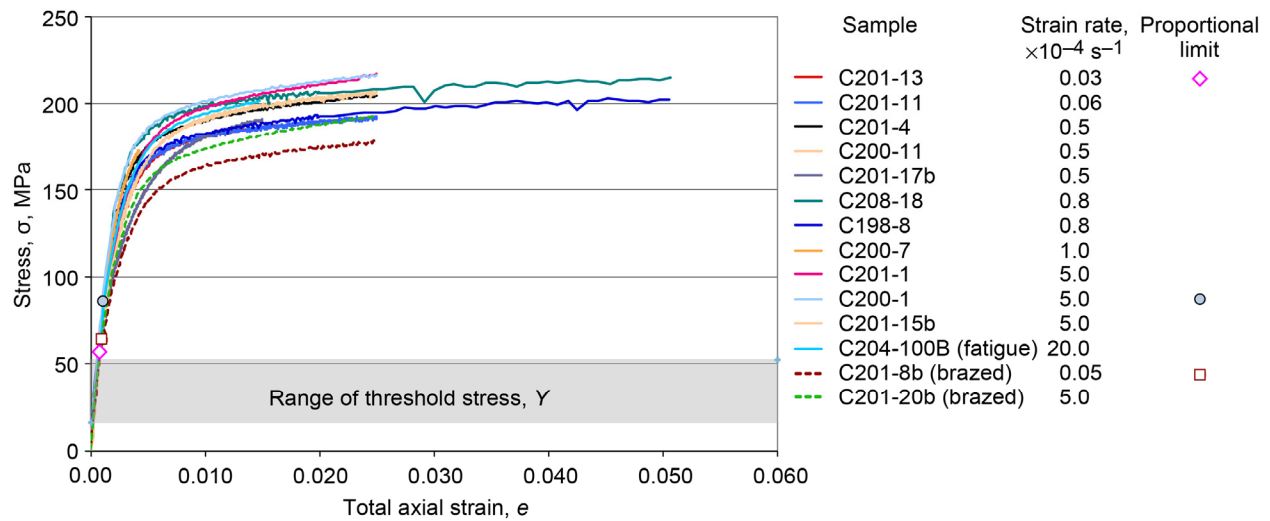


Figure 12.—Tensile stress-strain curves for GRCop-84 at 400 °C and different strain rates, showing range of threshold stress Y and proportional limits PL .

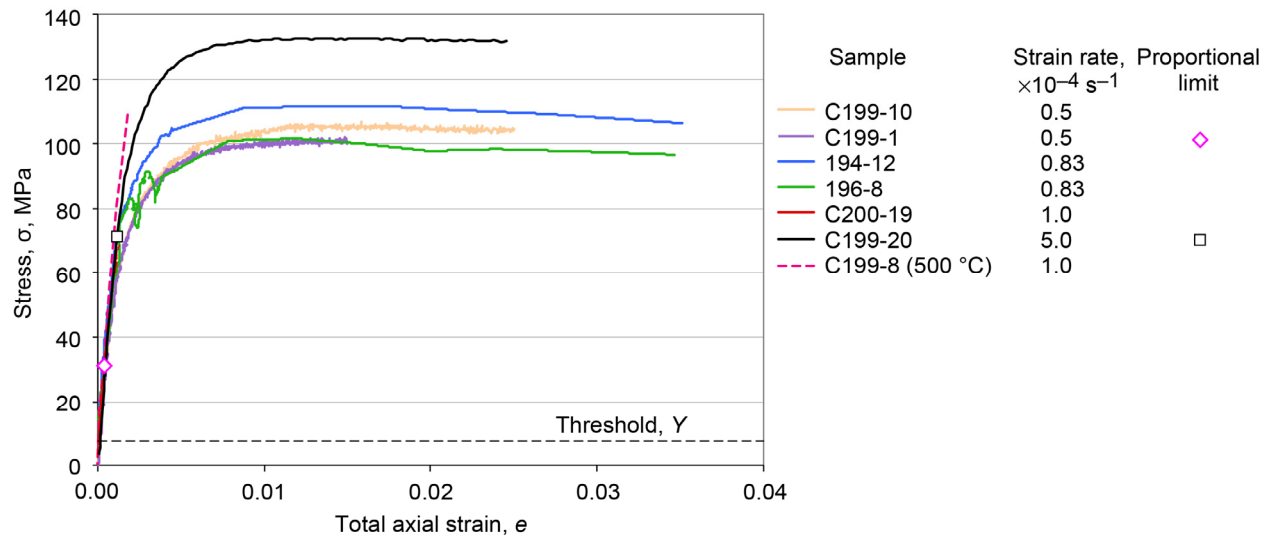


Figure 13.—Tensile stress-strain curves for GRCop-84 at 600 °C and different strain rates, showing threshold stress, Y and proportional limits PL .

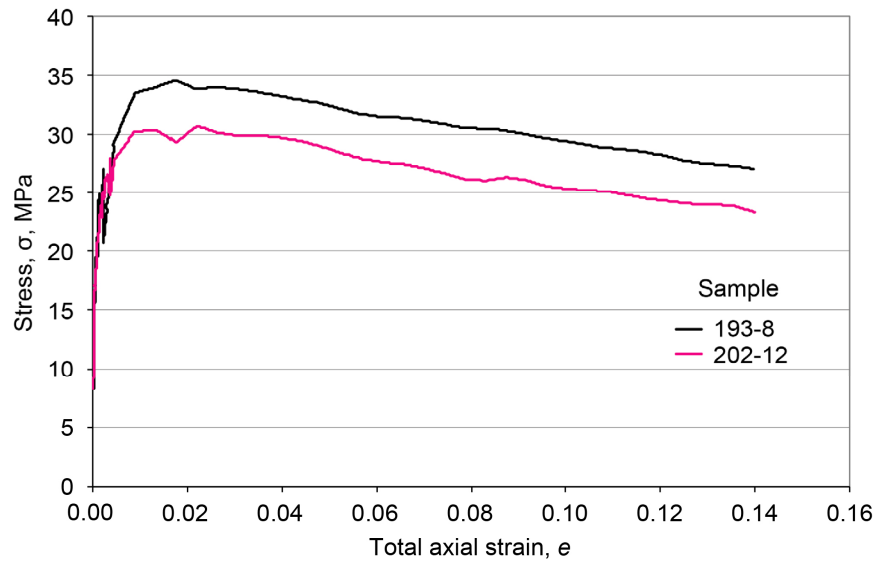


Figure 14.—Tensile stress-strain curves for GRCop-84 at 800 °C and strain rate of 0.000083 s^{-1} .

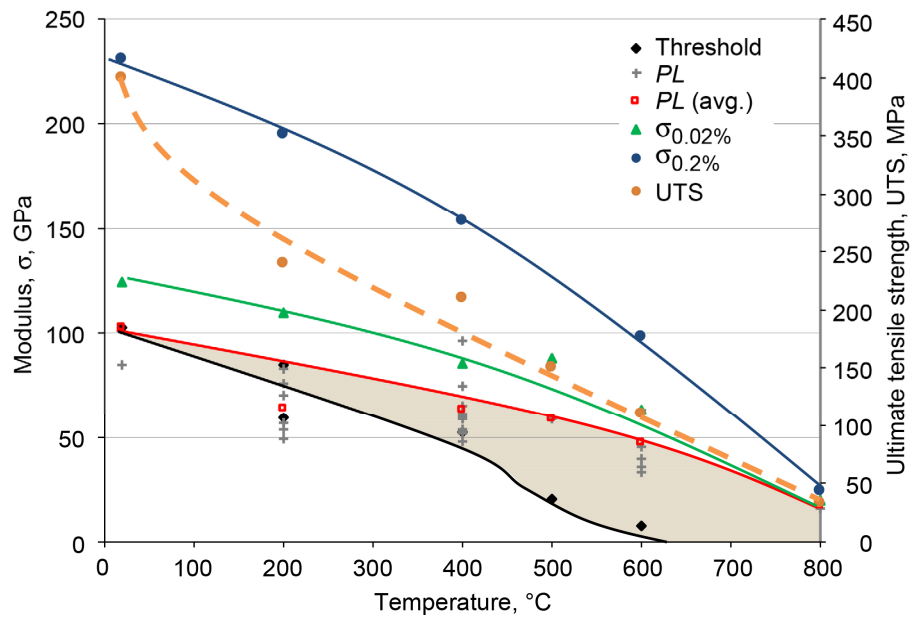


Figure 15.—GRCop-84 temperature dependence of 0.02 and 0.2 yield points $\sigma_{0.02\%}$ and $\sigma_{0.2\%}$ (strain rate = 0.0001 s^{-1}), UTS, threshold stress Y , and proportional limit PL .

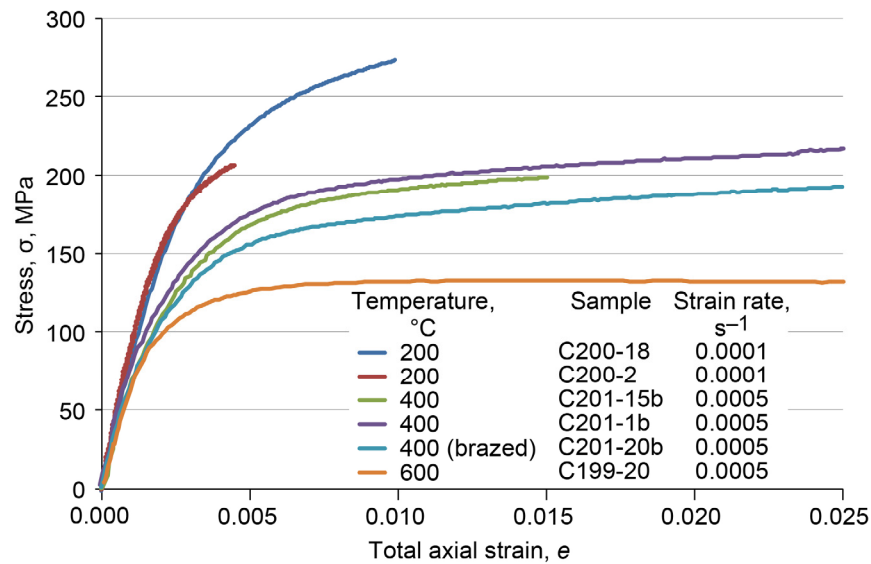


Figure 16.—Tensile stress-strain curves for GRCop-84 as function of temperature.

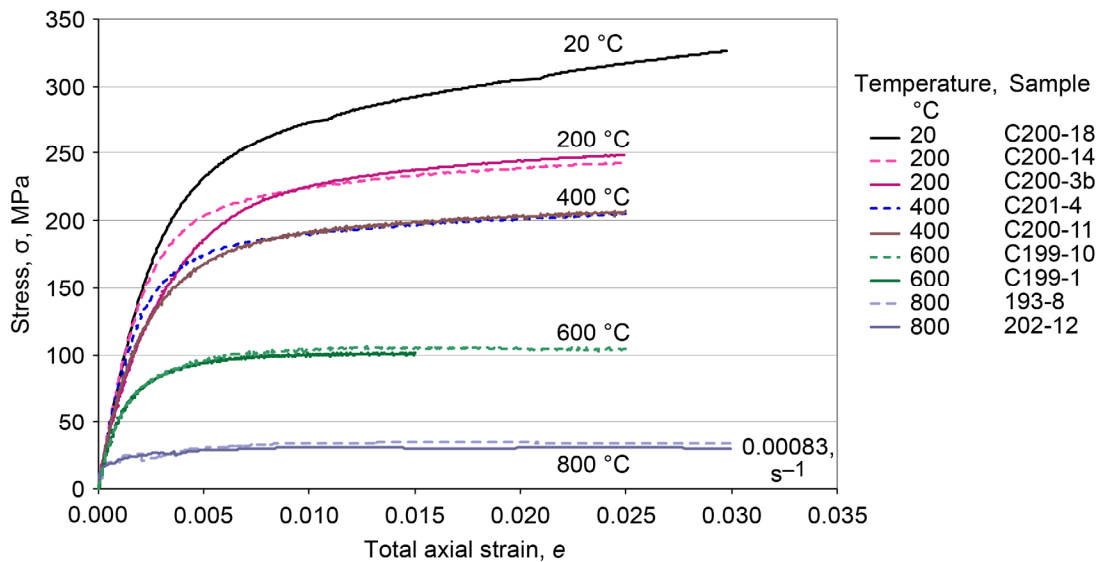


Figure 17.—Tensile stress-strain curves for GRCop-84 as function of temperature at slow strain rate, 0.00005 s⁻¹.

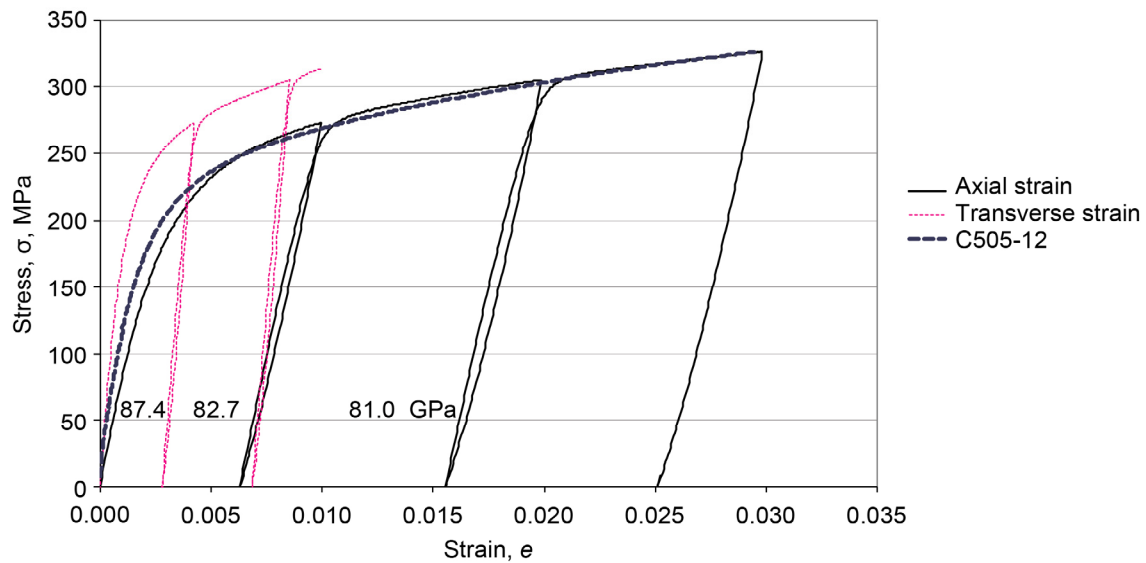


Figure 18.—Tensile stress-strain curves for GRCop-84 at 20 °C and strain rate of 0.0001 s^{-1} , showing unloads every 0.01 axial strain. Loading modulus is given for each cycle. Negative transverse strain is also plotted.

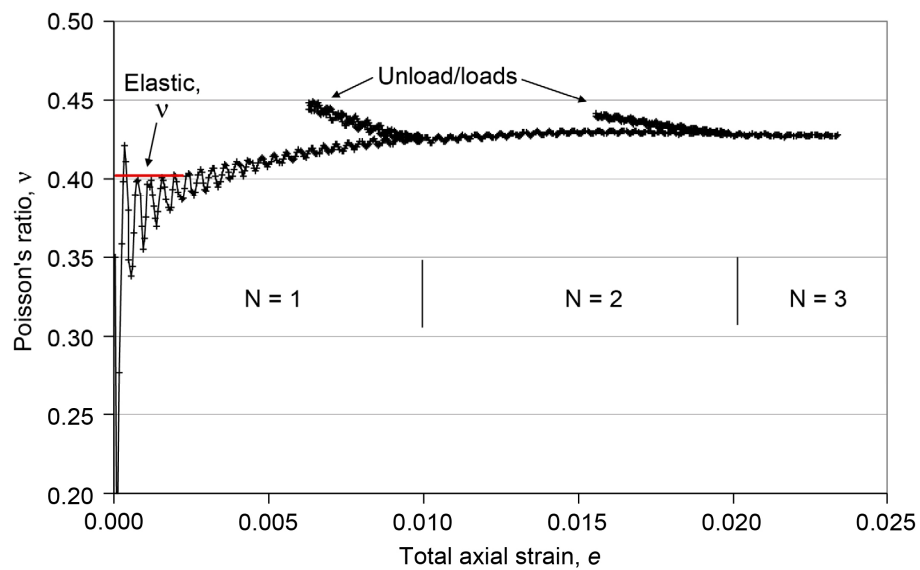


Figure 19.—Poisson's ratio for GRCop-84 sample C200-18 at 20 °C and strain rate of 0.0001 s^{-1} , showing three load-unload cycles N .

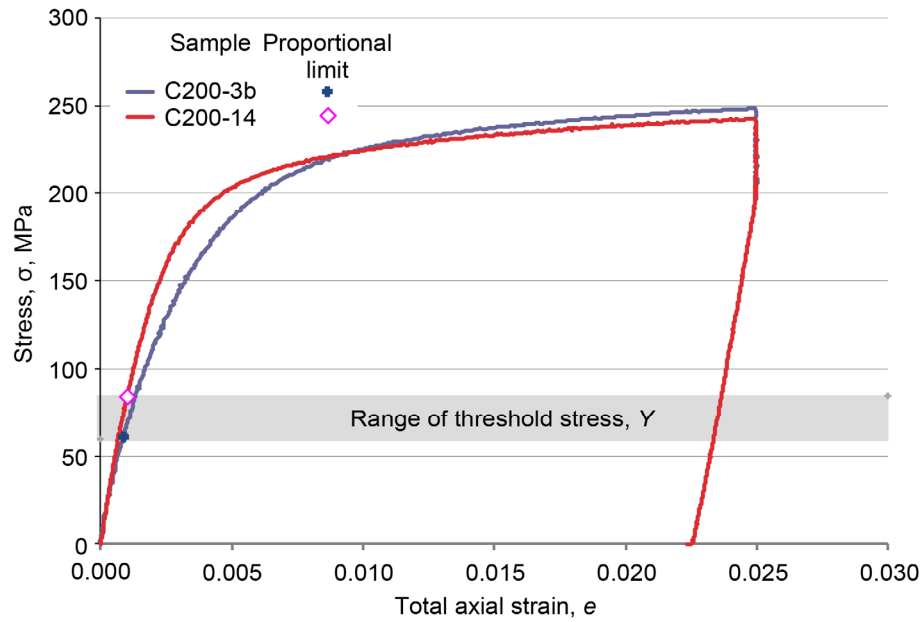


Figure 20.—Stress-strain curves for GRCop-84 at 200 °C and strain rate of 0.00005 s^{-1} for relaxation at 0.025 axial strain, showing range of threshold stress Y and proportional limits PL .

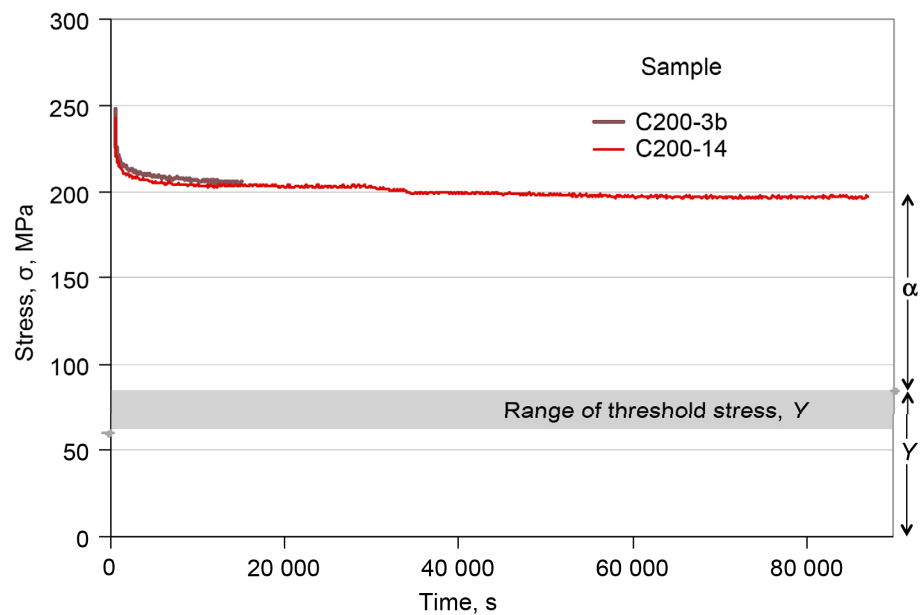


Figure 21.—Relaxation behavior for GRCop-84 at 200 °C, strain rate of 0.00005 s^{-1} , and strain of 0.025, showing range of threshold stress Y and back stress α .

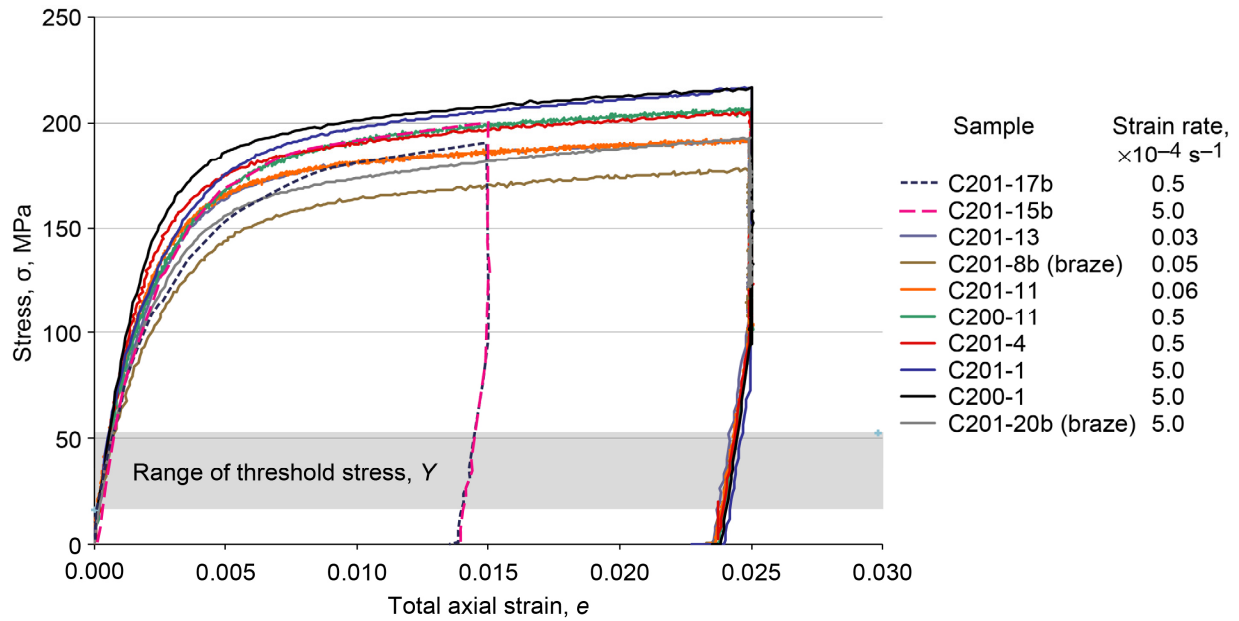


Figure 22.—Stress-strain curves for GRCop-84 at 400 °C and different strain rates for relaxations at 0.015 and 0.025 axial strain, showing range of threshold stress Y .

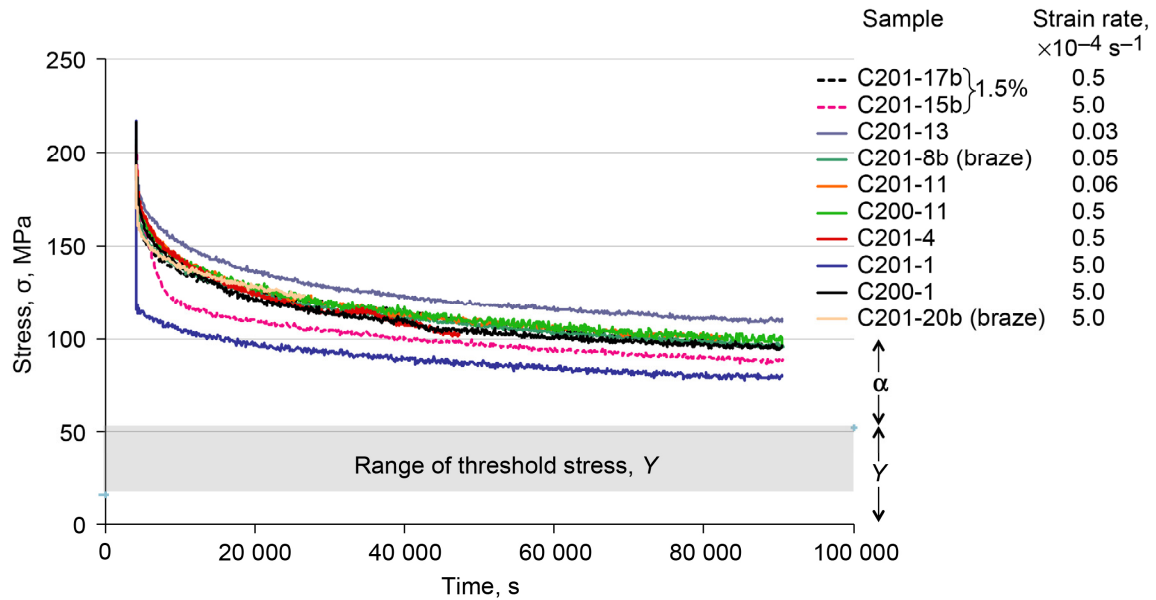


Figure 23.—Relaxation behavior for GRCop-84 at 400 °C, strains of 0.015 and 0.025, and different strain rates, showing range of threshold stress Y and back stress α . Times translated to account for length of loadup.

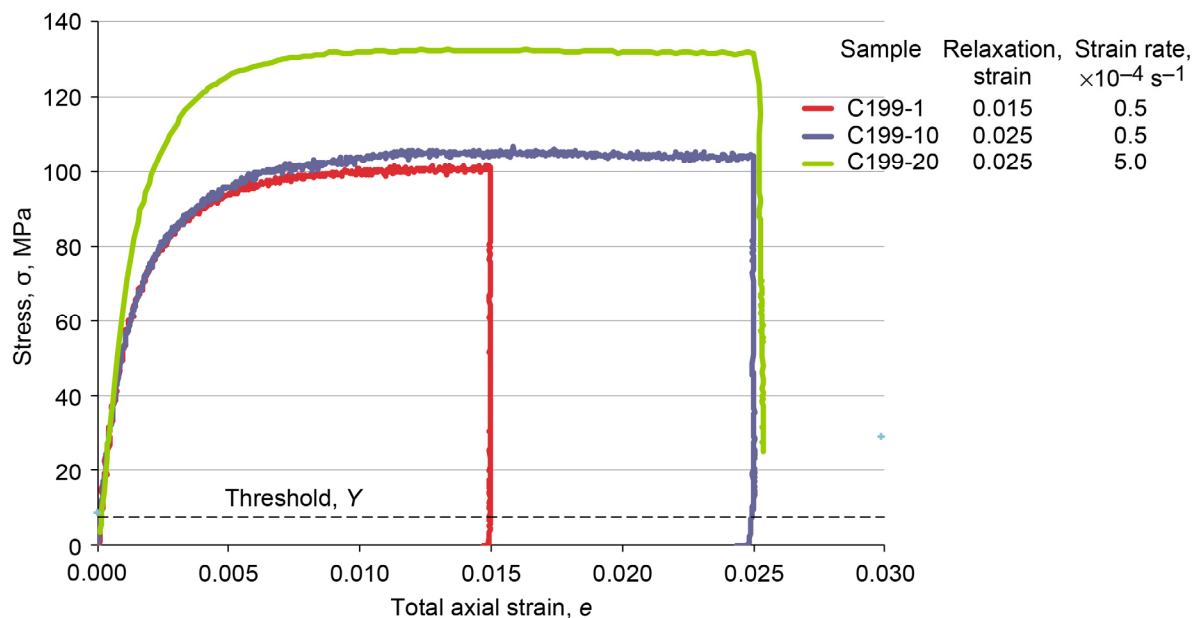


Figure 24.—Stress-strain curves for GRCop-84 at 600 °C and different strain rates for relaxations at 0.015 and 0.025 axial strain, showing threshold stress Y .

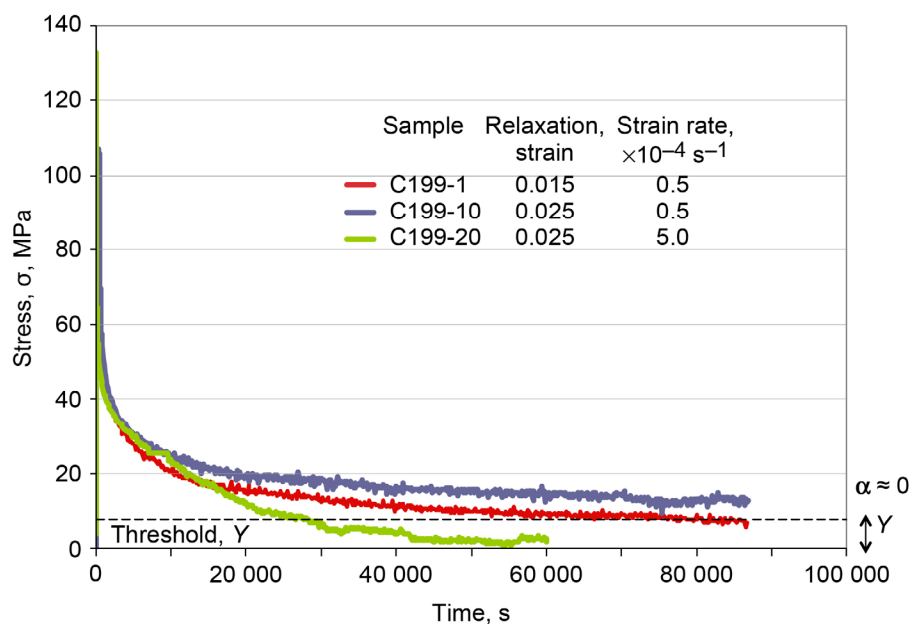


Figure 25.—Relaxation behavior for GRCop-84 at 600 °C, strain rates of 0.0005 and 0.00005 s^{-1} , and strains of 0.015 and 0.025, showing range of threshold stress Y and back stress α .

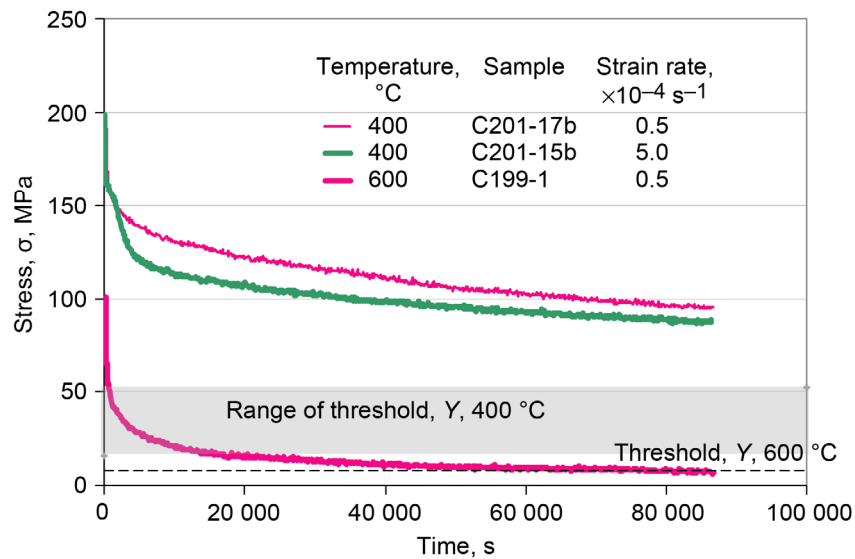


Figure 26.—Relaxation behavior for GRCop-84 at 400 and 600 °C, strain rates of 0.0005 and 0.00005 s^{-1} , and strain of 0.015, showing range of threshold stress Y at each temperature.

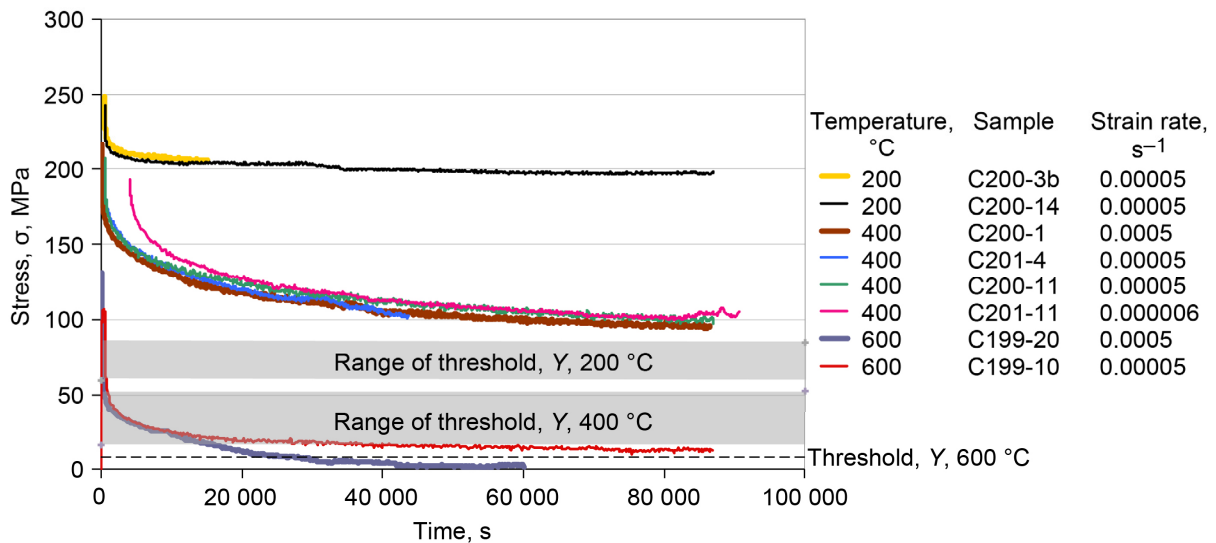


Figure 27.—Relaxation behavior for GRCop-84 at strain of 0.025 and various temperatures and strain rates, showing range of threshold stress Y at each temperature.

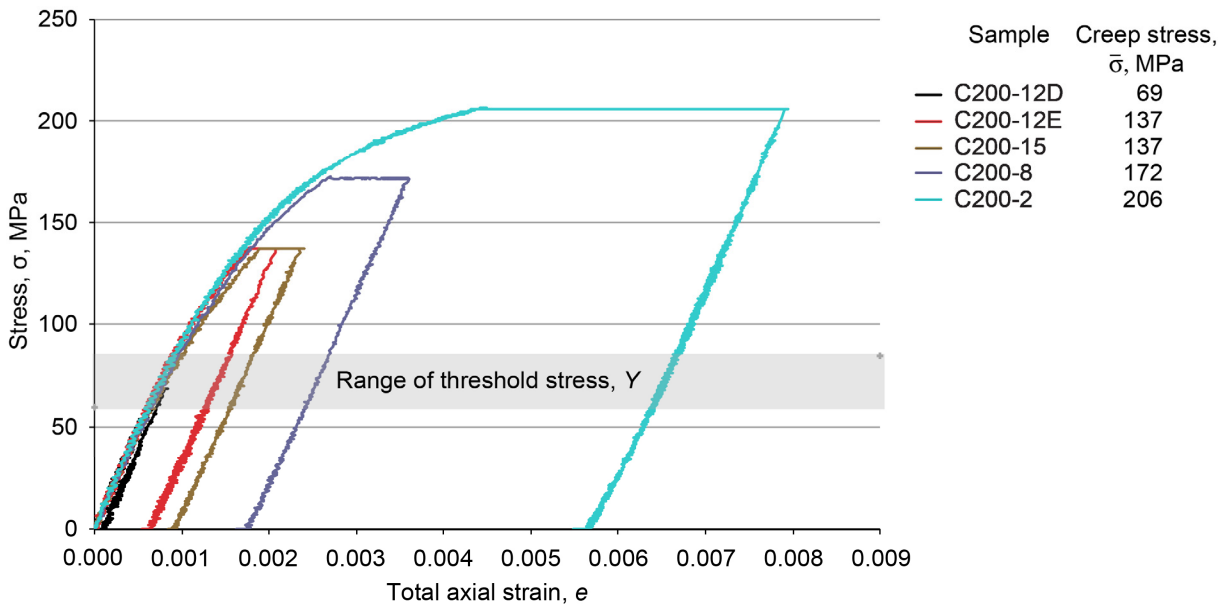


Figure 28.—Stress-strain curves for GRCop-84 for creep tests at 200 °C and strain rate of 0.0001 s^{-1} , showing range of threshold stress Y .

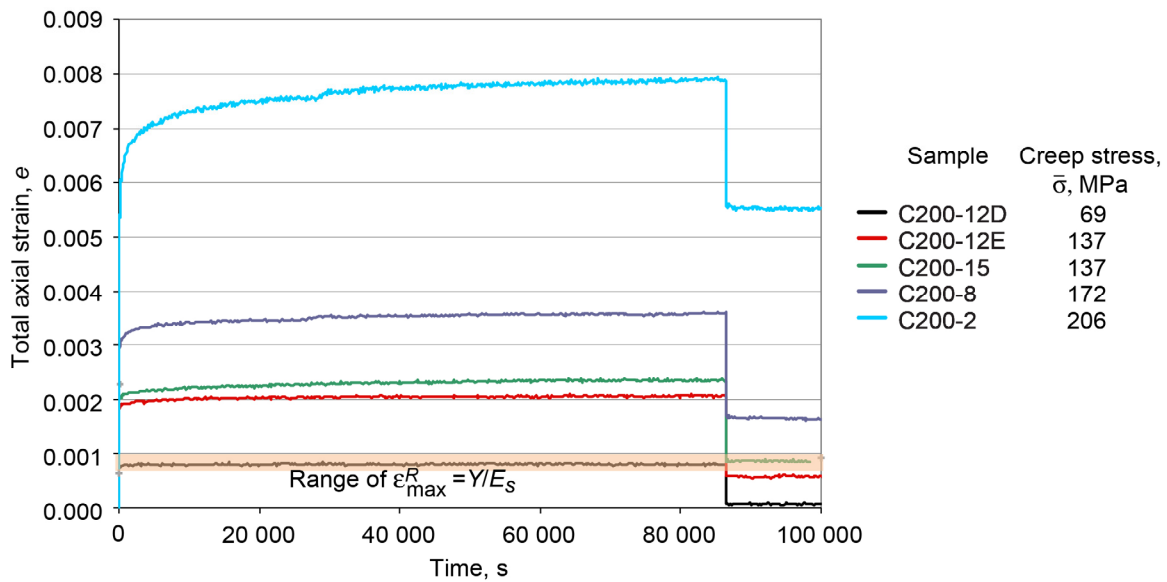


Figure 29.—Strain-time response of GRCop-84 for creep tests at various stress levels at 200 °C and strain rate of 0.0001 s^{-1} , with unload and recovery, showing range of maximum reversible strain ϵ_{\max}^R , where Y is threshold stress and E_s is infinitely slow modulus.

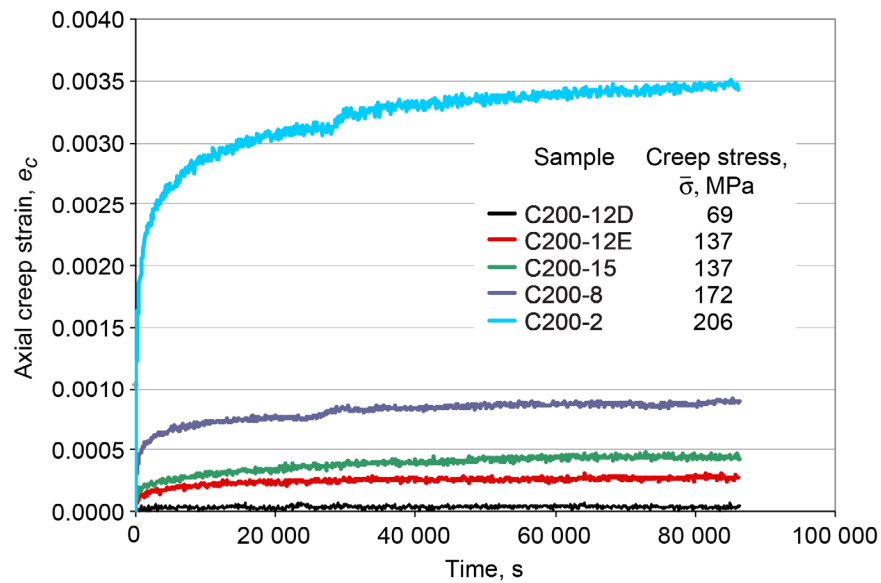


Figure 30.—Axial creep strain for GRCop-84 at various stress levels at 200 °C and strain rate of 0.0001 s^{-1} .

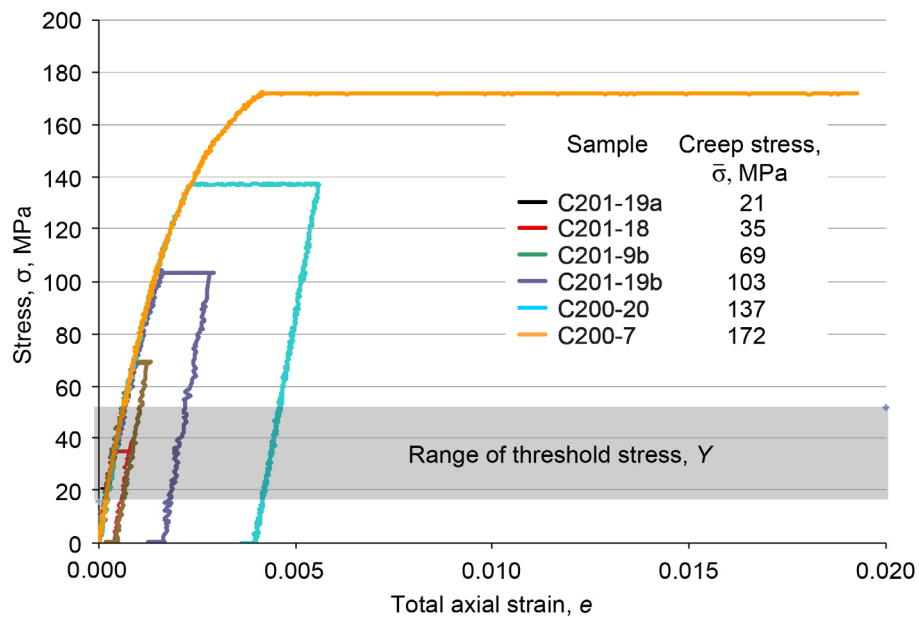


Figure 31.—Stress-strain curves for GRCop-84 for creep tests at various stress levels at 400 °C and strain rate of 0.0001 s^{-1} , showing range of threshold stress Y .

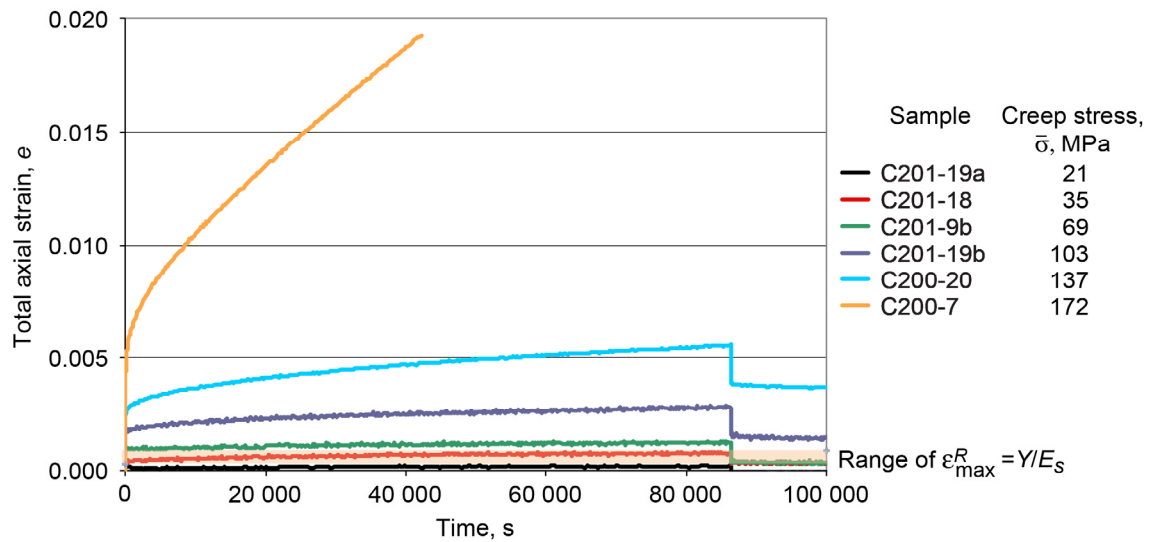


Figure 32.—Strain-time response of GRCop-84 for creep tests at various stress levels at 400 °C and strain rate of 0.0001 s^{-1} , with unload and recovery, showing range of maximum reversible strain ϵ_{\max}^R , where Y is threshold stress and E_s is infinitely slow modulus.

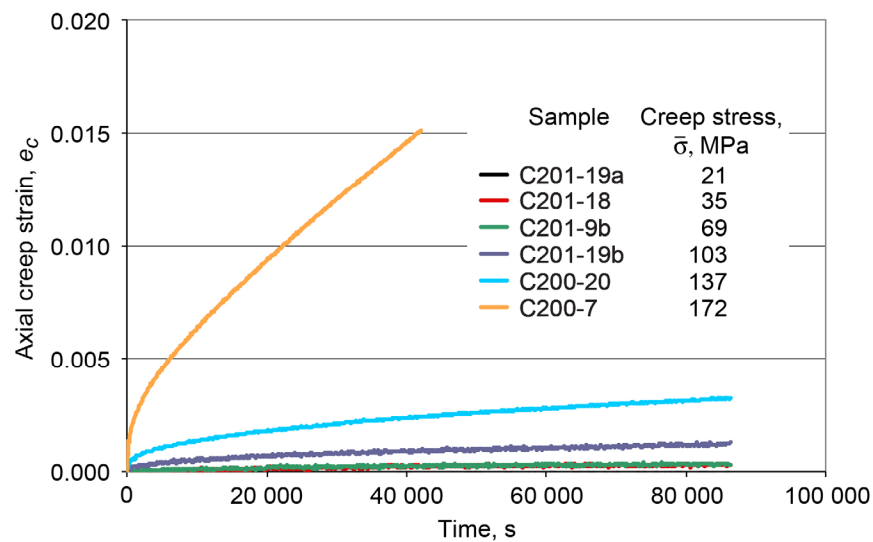


Figure 33.—Axial creep strain for GRCop-84 at various stress levels at 400 °C and strain rate of 0.0001 s^{-1} .

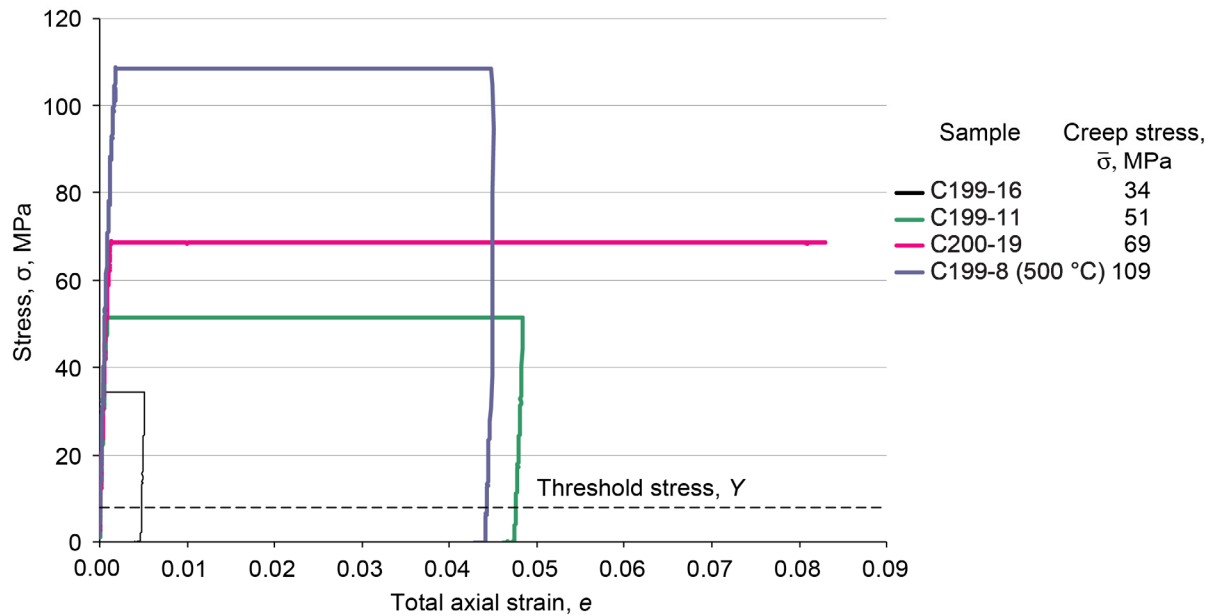


Figure 34.—Stress-strain curves for GRCop-84 for creep tests at various stress levels at 600 °C and strain rate of 0.0001 s^{-1} , showing threshold stress Y . Compared with creep test at 500 °C.

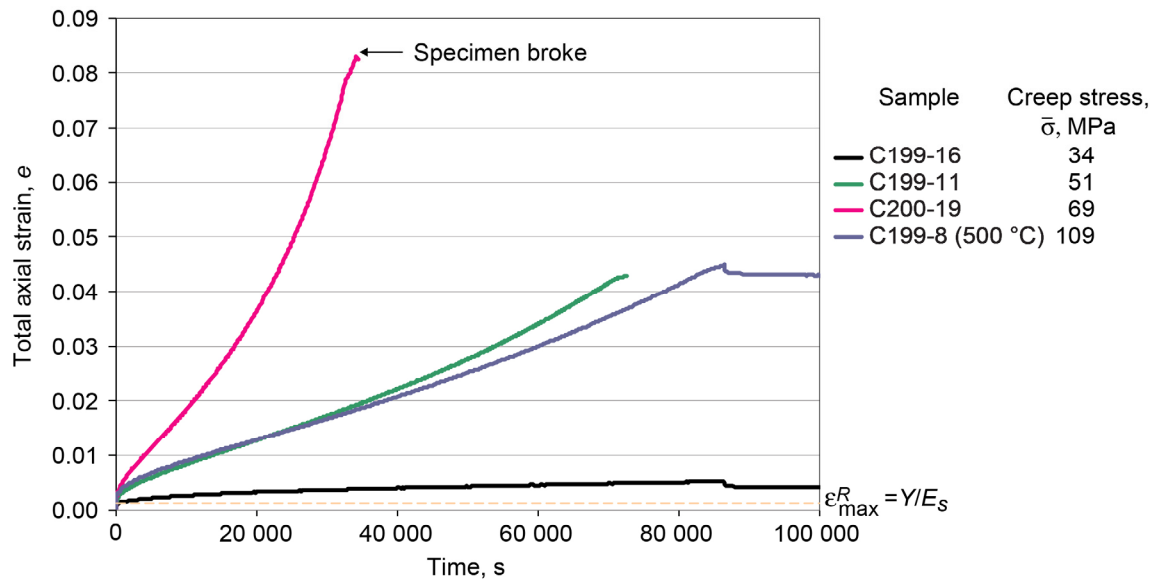


Figure 35.—Strain-time response of GRCop-84 for creep tests at various stress levels at 600 °C and strain rate of 0.0001 s^{-1} with unload and recovery, showing maximum reversible strain ϵ_{\max}^R , where Y is threshold stress and E_s is infinitely slow modulus. Compared with creep test at 500 °C.

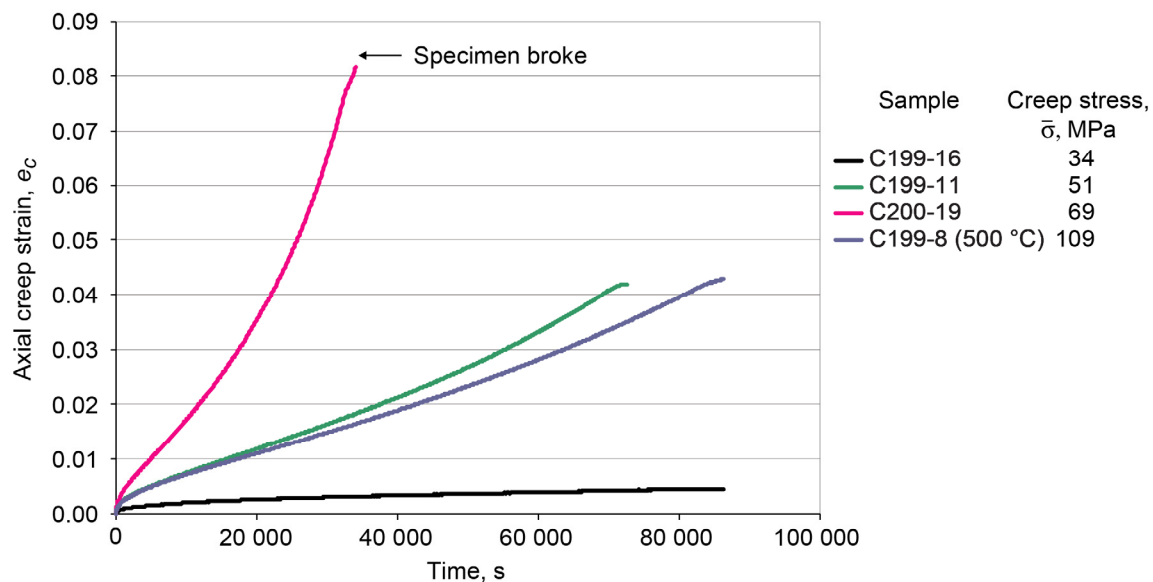


Figure 36.—Axial creep strain for GRCop-84 at various stress levels at 600 °C and strain rate of 0.0001 s^{-1} compared with creep test at 500 °C.

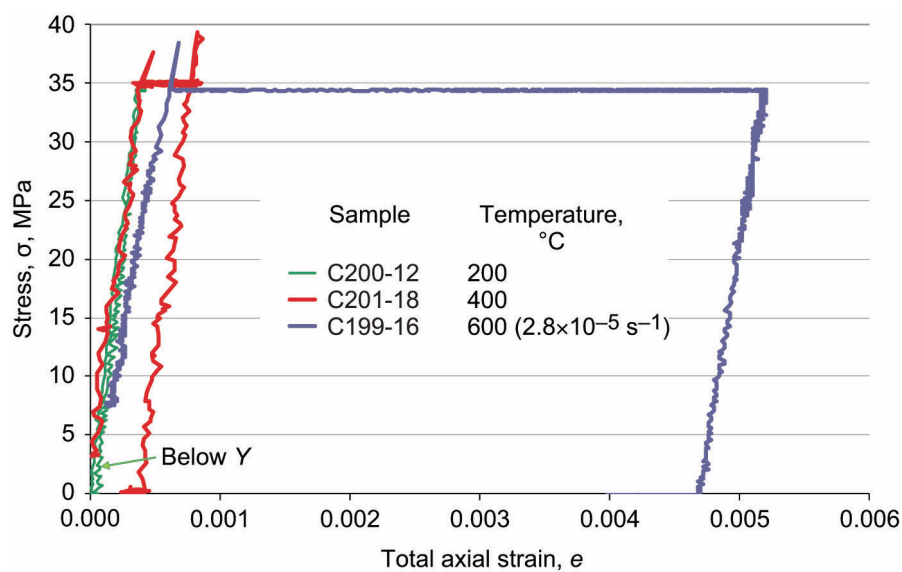


Figure 37.—Stress-strain curves for GRCop-84 creep tests at 34 MPa stress at various temperatures and strain rate of 0.0001 s^{-1} . Y is threshold stress.

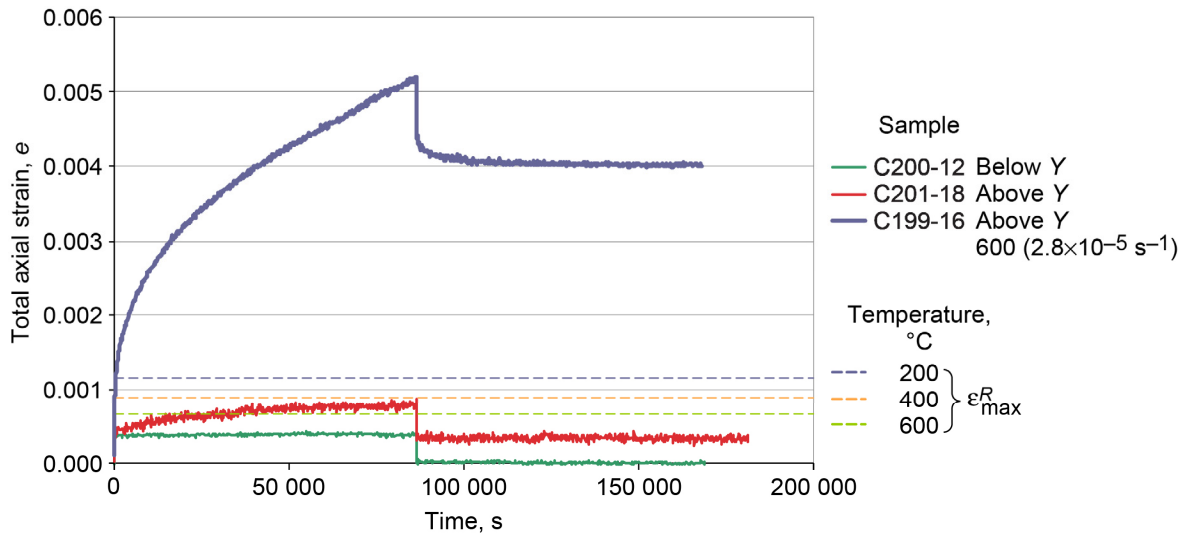


Figure 38.—Strain-time response of GRCop-84 at various temperatures at creep stress of 34 MPa and strain rate of 0.0001 s^{-1} with unload and recovery, showing maximum reversible strain ϵ_{\max}^R . Y is threshold stress.

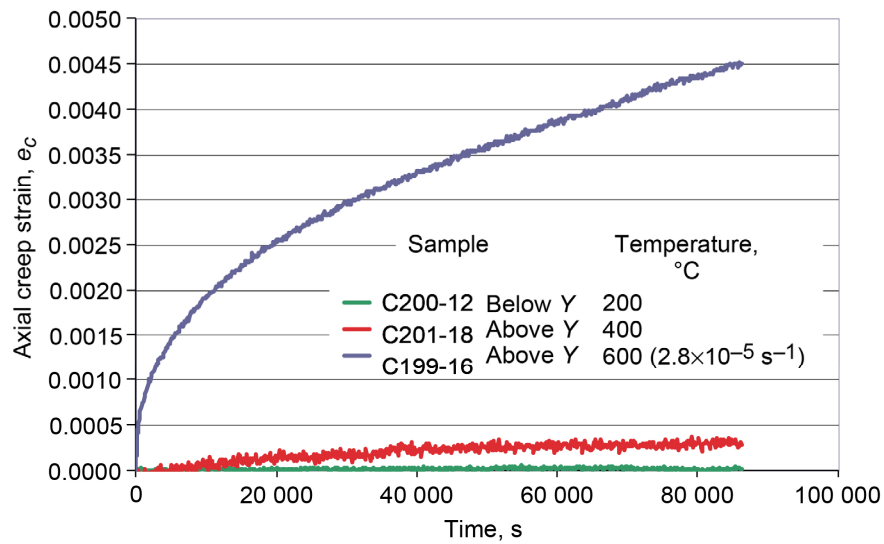


Figure 39.—Axial creep strain for GRCop-84 at various temperatures at creep stress of 34 MPa and strain rate of 0.0001 s^{-1} . Y is threshold stress.

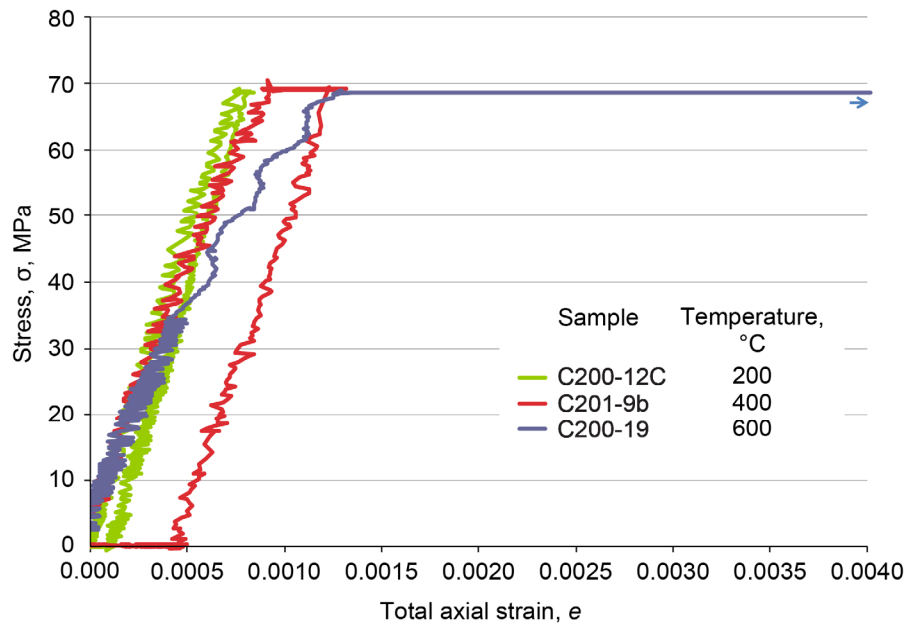


Figure 40.—Stress-strain curves for GRCop-84 at creep stress of 69 MPa at various temperatures and strain rate of 0.0001 s^{-1} . All tests are above threshold stress Y .

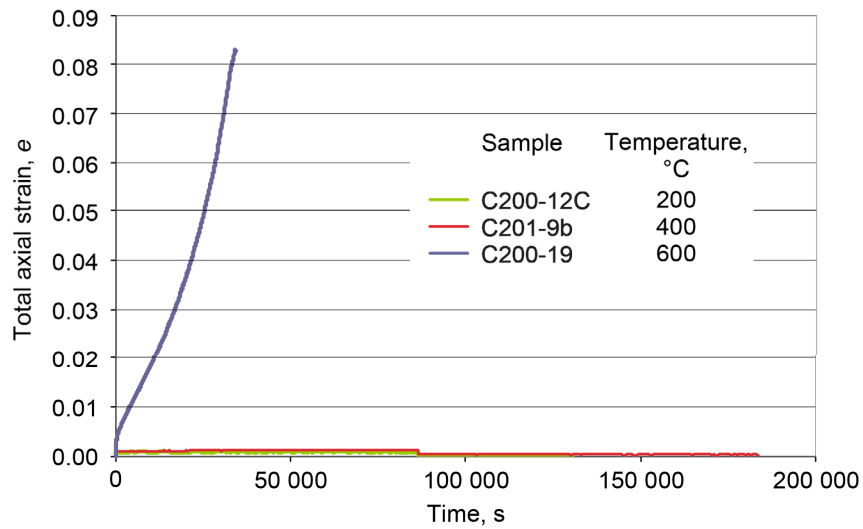


Figure 41.—Strain-time response of GRCop-84 at creep stress of 69 MPa at various temperatures and strain rate of 0.0001 s^{-1} , with unload and recovery. All tests are above threshold stress Y .

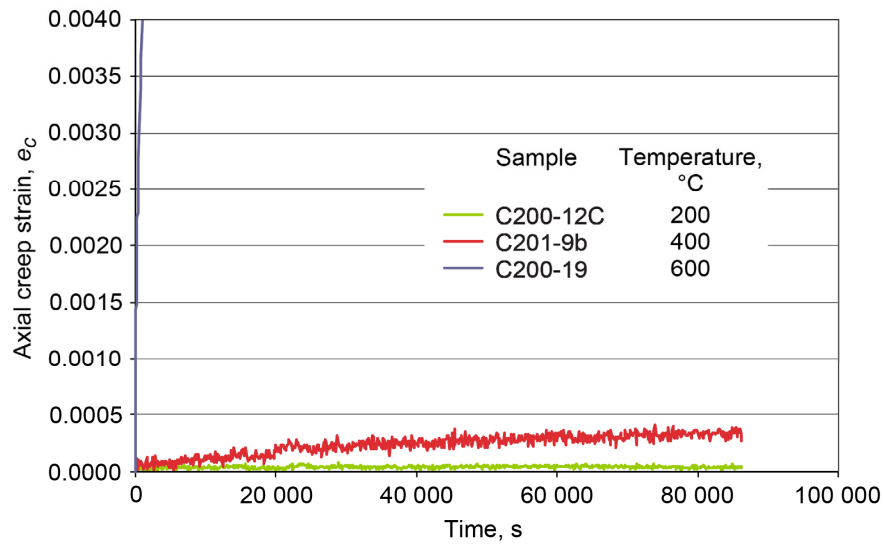


Figure 42.—Axial creep strain for GRCop-84 at stress level of 69 MPa at various temperatures and strain rate of 0.0001 s^{-1} . All tests are above threshold stress Y .

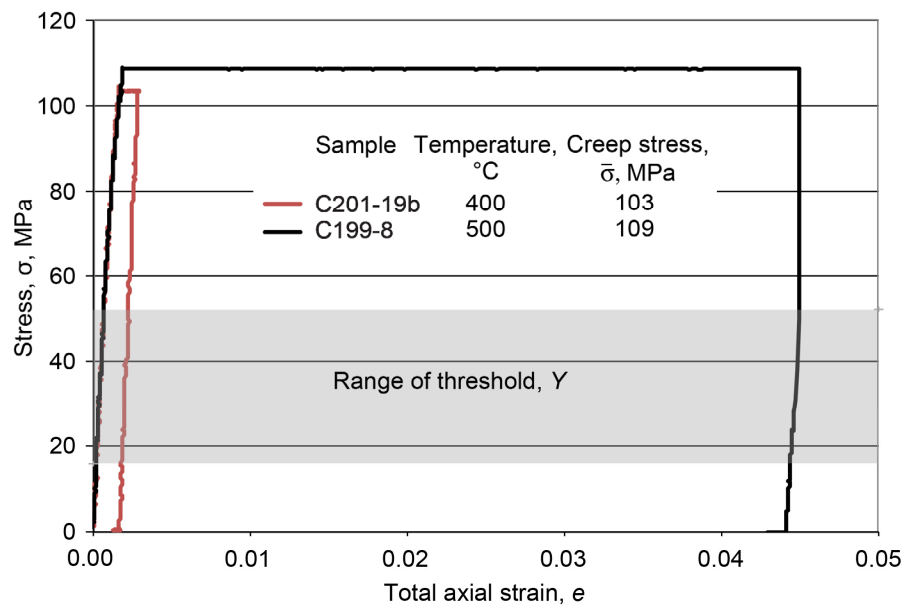


Figure 43.—Stress-strain curves for GRCop-84 at creep stresses $\bar{\sigma}$ of 103 and 109 MPa at 400 and 500 °C, respectively, and strain rate of 0.0001 s^{-1} , showing range of threshold stress Y .

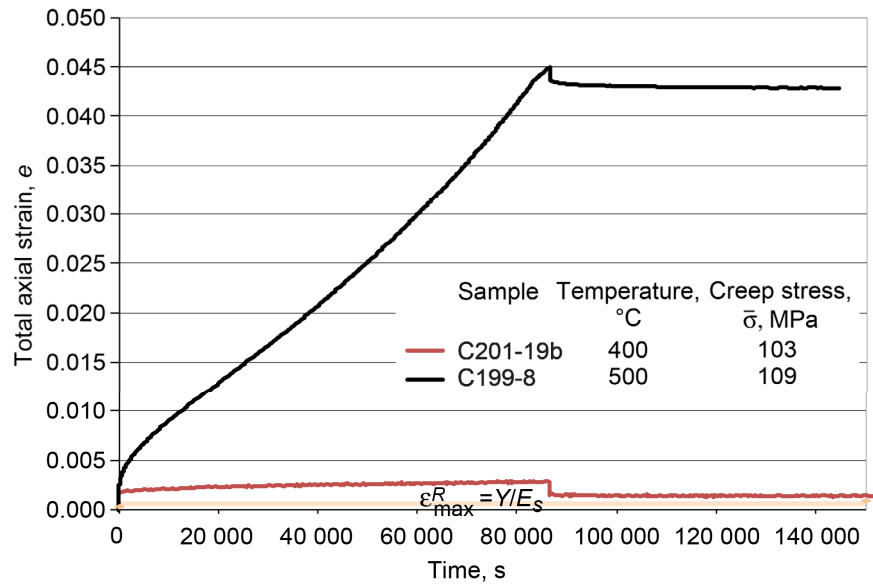


Figure 44.—Strain-time response of GRCop-84 at creep stress of 103 and 109 MPa at 400 and 500 °C, respectively, and strain rate of 0.0001 s^{-1} with unload and recovery, showing range of maximum reversible strain ϵ_{\max}^R , where Y is threshold stress and E_s is infinitely slow modulus.

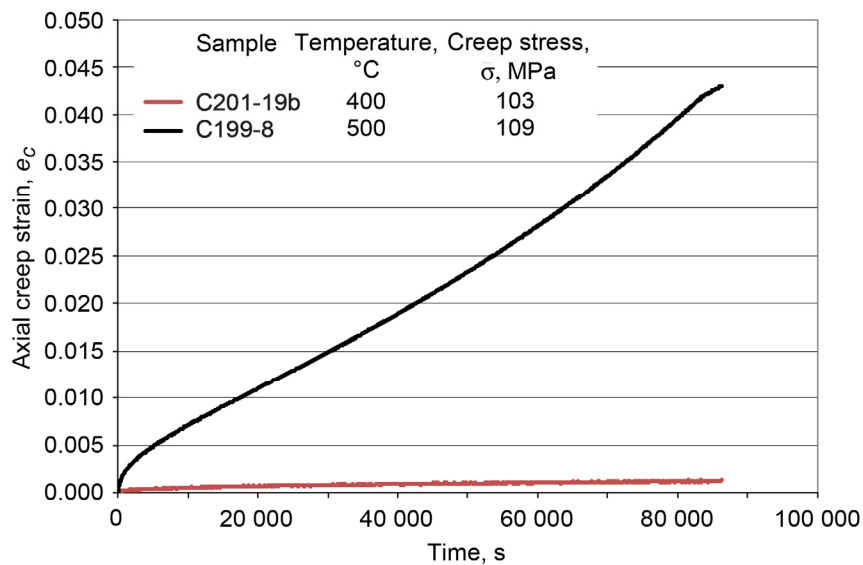


Figure 45.—Axial creep strain for GRCop-84 at 103 and 109 MPa at 400 and 500 °C, respectively, and strain rate of 0.0001 s^{-1} .

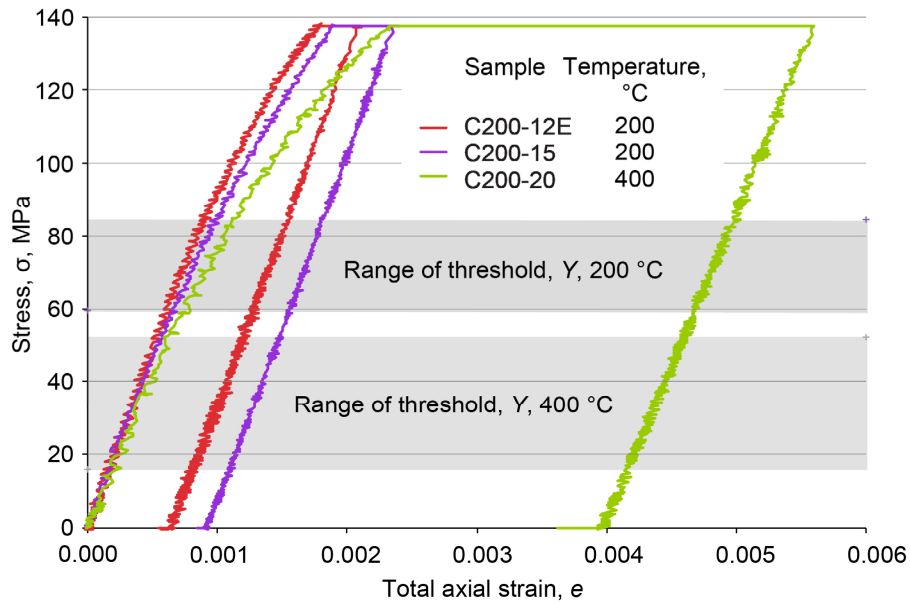


Figure 46.—Stress-strain curves for GRCop-84 at creep stress of 137 MPa at various temperatures and strain rate of 0.0001 s^{-1} , showing range of threshold stress Y .

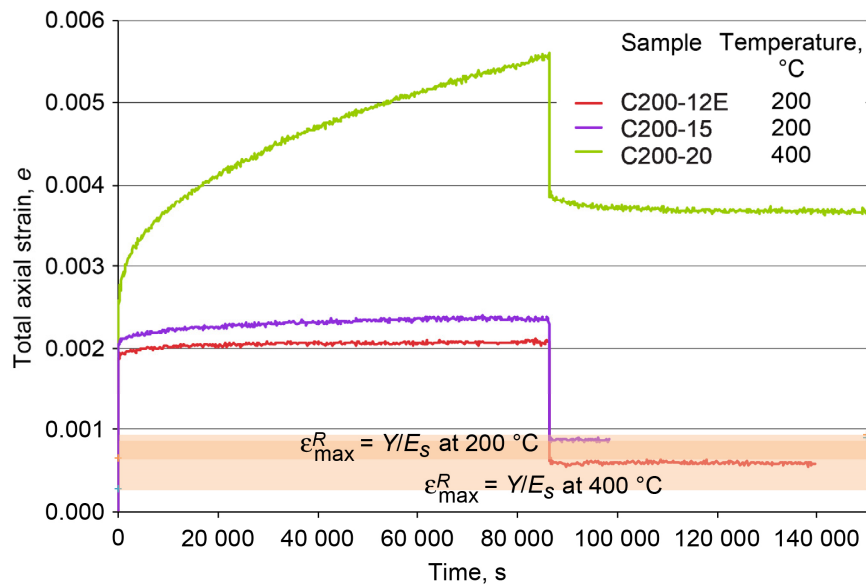


Figure 47.—Strain-time response of GRCop-84 at creep stress of 137 MPa at 200 and 400 °C and strain rate of 0.0001 s^{-1} with unload and recovery, showing maximum reversible strain ϵ_{\max}^R , where Y is threshold stress and E_s is infinitely slow modulus.

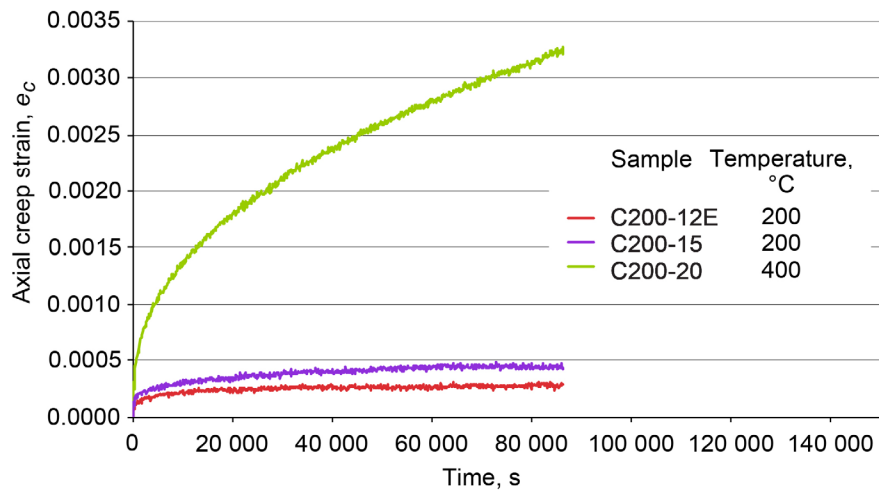


Figure 48.—Axial creep strain for GRCop-84 at 137 MPa at 200 and 400 °C and strain rate of 0.0001 s^{-1} .

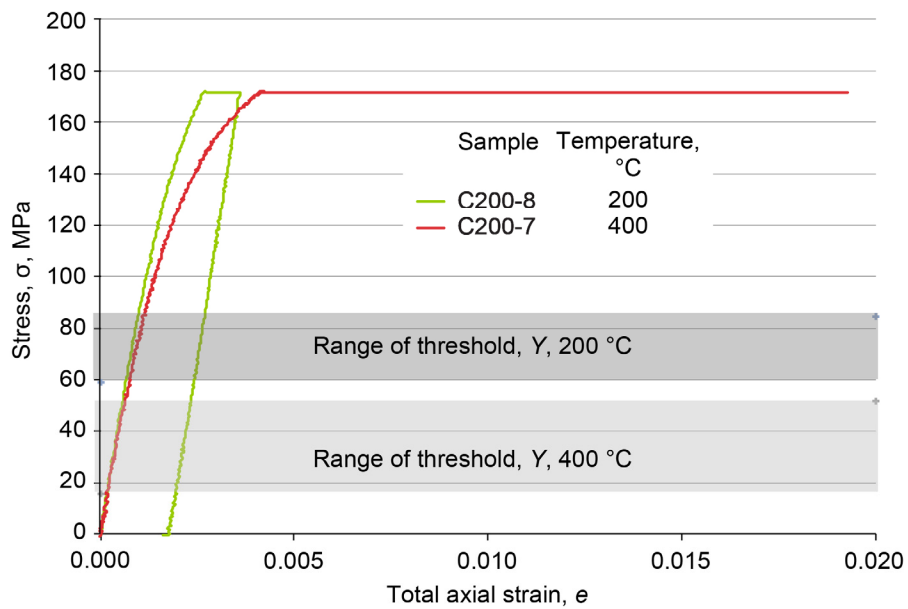


Figure 49.—Stress-strain curves for GRCop-84 at creep stress of 172 MPa at 200 and 400 °C and strain rate of 0.0001 s^{-1} , showing range of threshold stress Y .

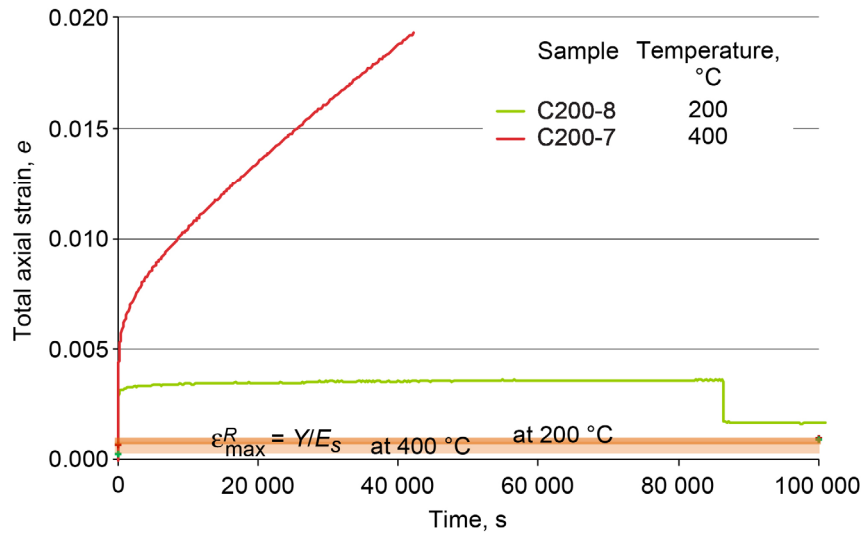


Figure 50.—Strain-time response of GRCop-84 at creep stress of 172 MPa at 200 and 400 °C and strain rate of 0.0001 s^{-1} with unload and recovery, showing maximum reversible strain ϵ_{\max}^R , where Y is threshold stress and E_s is infinitely slow modulus.

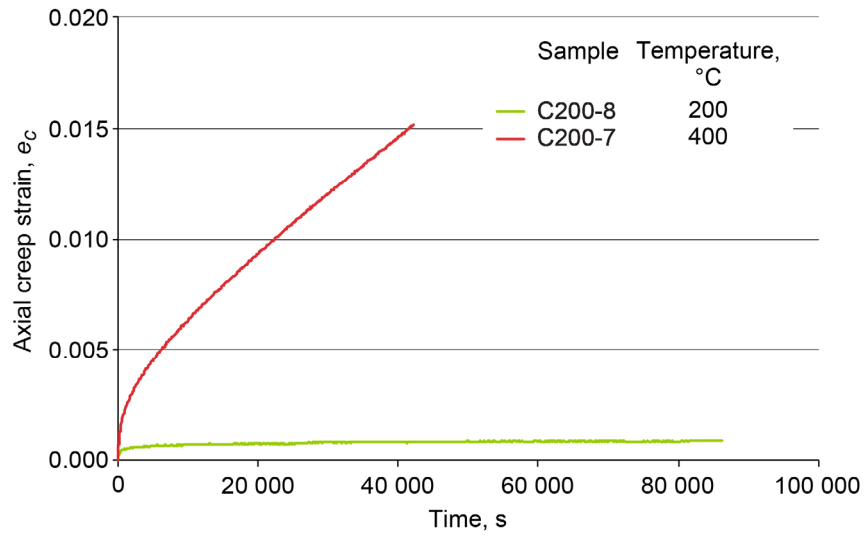


Figure 51.—Axial creep strain for GRCop-84 at various temperatures and 172 MPa at 200 and 400 °C and strain rate of 0.0001 s^{-1} .

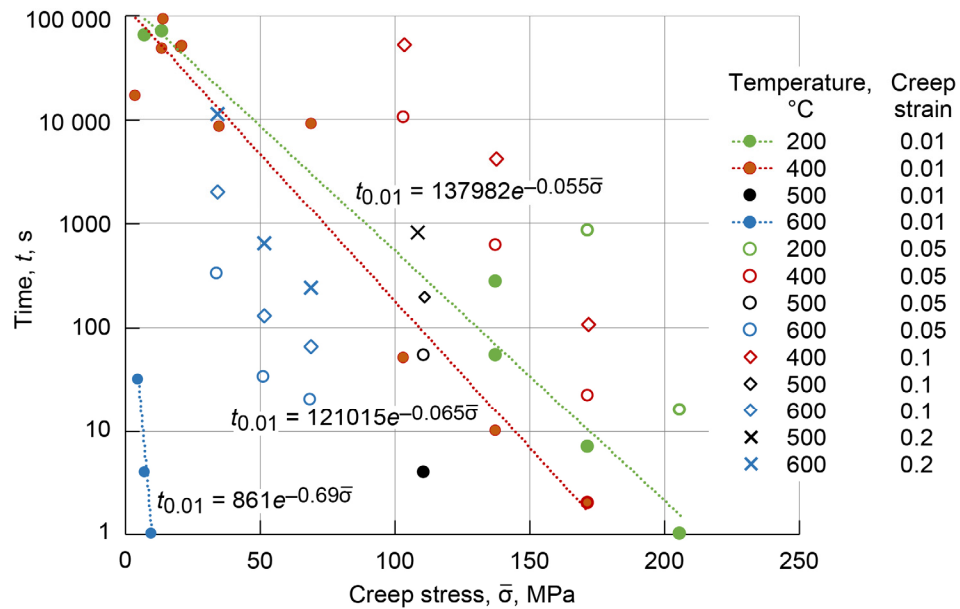


Figure 52.—Time to various creep strains for GRCop-84 at various temperatures, with linear fits for creep strains of 0.01 percent.

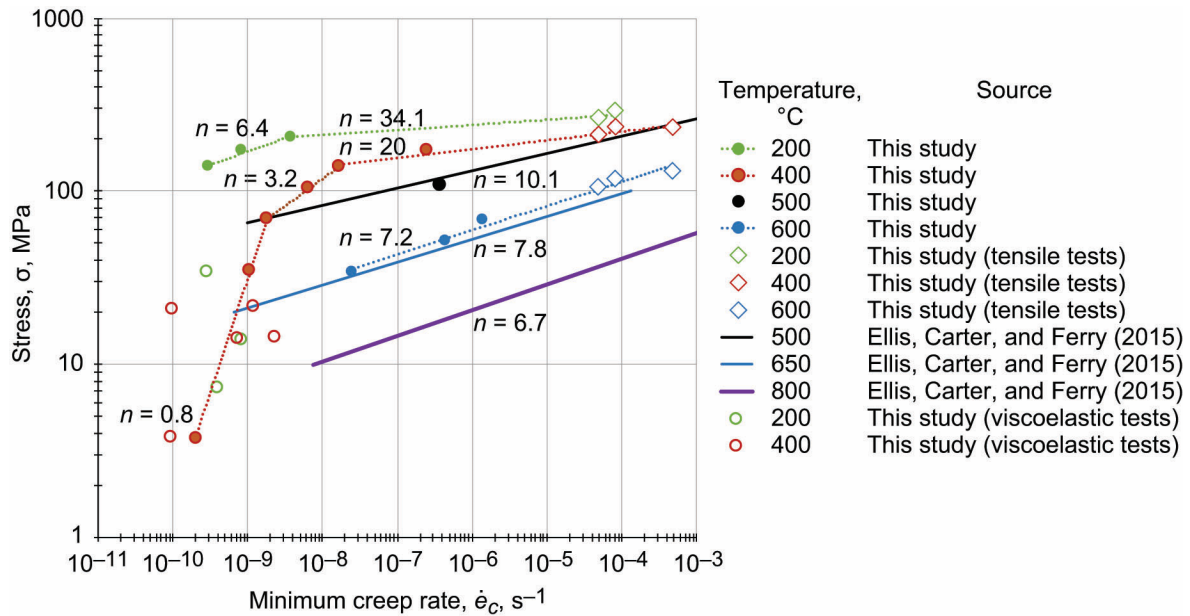


Figure 53.—Stress dependence on minimum creep rate for GRCop-84 at various temperatures, showing creep exponent, n . Comparison with line fits from Ellis, Carter, and Ferry (2015).

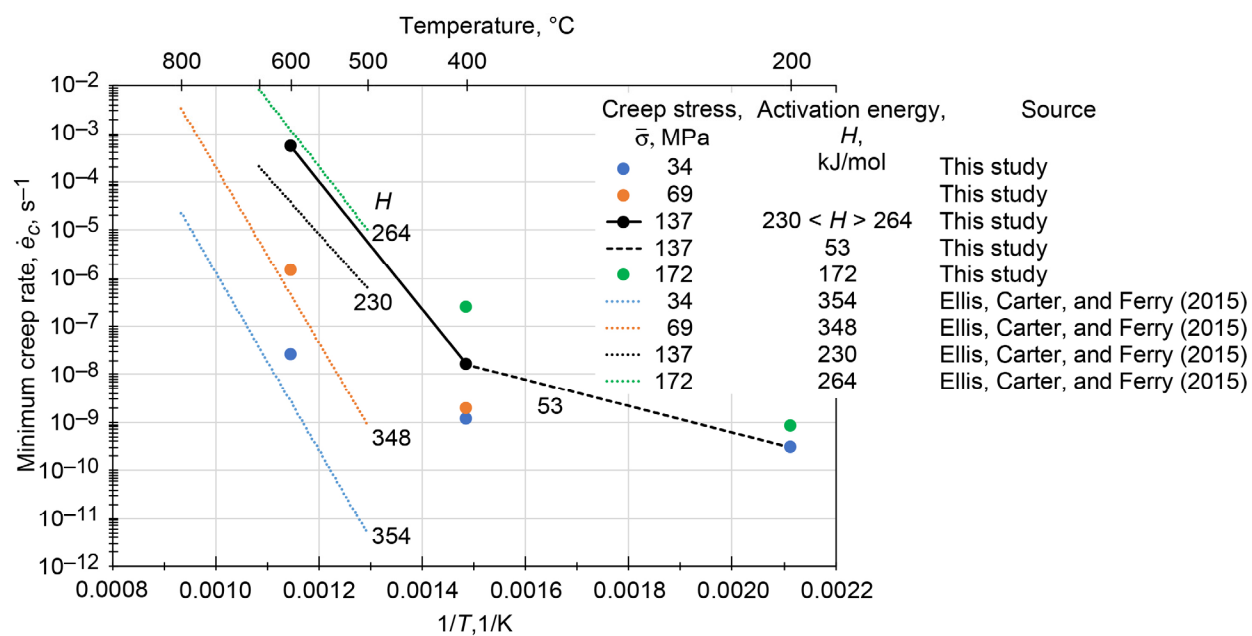


Figure 54.—Creep activation energy H for GRCop-84. Comparison with line fits from Ellis, Carter, and Ferry (2015).

